Available online at www.sciencedirect.com
ScienceDirect
Journal of Computational Physics 227 (2008) 1809–1835
JOURNAL OF COMPUTATIONAL PHYSICS
www.elsevier.com/locate/jcp

Spectral element method in time for rapidly actuated systems

Mohammad H. Kurdi *,[1], Philip S. Beran

AFRL/VASD, Building 146, 2210 8th Street, Wright-Patterson AFB, OH 45433, United States

Received 8 January 2007; received in revised form 27 September 2007; accepted 30 September 2007
Available online 24 October 2007

Abstract

In this paper, the spectral element (SE) method is applied in time to find the entire time-periodic or transient solution of time-dependent differential equations. The time-periodic solution is computed by enforcing periodicity of the element set. Of particular interest are periodic forcing functions possessing high frequency content. To maintain the spectral accuracy for such forcing functions, an *h*-refinement scheme is employed near the semi-discontinuity without increasing the number of degrees of freedom.

Time discretization by spectral elements is applied initially to a standard form of a set of linear, first-order differential equations subject to harmonic excitation and an excitation admitting rapid variation. Other case studies include the application of the SE approach to parabolic and hyperbolic partial differential equations. The first-order form of these equations is obtained through semi-discretization using conventional finite-element, spectral element and finite-difference schemes. Element clustering (*h*-refinement) is applied to maintain the high accuracy and efficiency in the region of the forcing function admitting rapid variation. The convergence in time of the method is demonstrated. In some cases, machine precision is obtained with 25 degrees of freedom per cycle. Finally the method is applied to a weakly nonlinear problem with time-periodic solution to demonstrate its future applicability to the analysis of limit-cycle oscillations in aeroelastic systems.

Published by Elsevier Inc.

PACS: 65D30; 65M06; 65M70; 65M60; 74H45

Keywords: Spectral element; Time periodicity; Rapid excitation; Limit-cycle oscillations; Transient response; Aeroacoustic; Wave equation

1. Introduction

The analysis of transient and time-periodic response of systems to excitations has a wide variety of engineering applications. Typical examples include analysis of flutter and self-excited oscillations (limit-cycles) in many applications including aerospace [1,2], milling [3,4] and the convection–diffusion reaction in reactors

* Corresponding author. Tel.: +1 937 310 7469; fax: +1 937 656 4945.
E-mail address: mhkurdi@ufl.edu (M.H. Kurdi).

[1] This research was performed while the author held a National Research Council Research Associateship Award at the Air Force Research Laboratory.

0021-9991/$ - see front matter Published by Elsevier Inc.
doi:10.1016/j.jcp.2007.09.031

[5,6], to name but a few. The efficient and accurate time-dependent solution of these problems is of high interest.

Time calculations of differential equations are typically computed through time-marching schemes that employ finite-difference or finite-element approximations in time. These schemes offer a memory efficient computation of the time response by retaining only the current time calculation. The memory efficiency gained, however, introduces a weak connection between the unsteady (transient) solution and the system parameters, in which, sensitivity information can only be computed at local-time. Furthermore, time-marching schemes are inherently ill-suited for computing time-periodic solutions of periodically excited differential equations. This deficiency materializes when the solution is time-marched for a number of cycles until the time-periodic solution is obtained.

An alternative to time-marching schemes is the use of space–time finite-elements to discretize the entire time domain. This was first proposed by Oden [7], Desai et al. [8], Fried [9], Argyris and Scharpf [10]. The underlying discretization was based on the use of Hamilton principle for dynamics. In this paper we use spectral elements (SEs) to approximate the time derivative operator where the entire time-dependent solution is computed using a single monolithic-time calculation. The monolithic-time interval would encompass the entire transient and time-periodic responses.

Although the monolithic-time approach may have some limitations especially for hyperbolic problems, it does offer some advantages warranting the investigation. Particularly, the global-time projection of the response, transforms the time dependent differential equation into an algebraic form, which in contrast to time-marching, presents a strong connection between the unsteady (transient) solution and the system parameters. One example application where this is beneficial is in the optimal control of limit-cycle oscillations (LCOs) in aircrafts [11,12] where the sensitivity of the LCO amplitude can be computed for global-time. Additionally, a more efficient solution is found when the SE in monolithic-time is applied to differential equations with periodic excitations, for which only the time-periodic response is of interest. In this case, the monolithic-time interval is equal to the whole cycle. The method proves to be more efficient as the solution does not need to march in time through the transients to reach the time-periodic solution.

The SE method was introduced by Patera [13] to approximate the spatial derivative operator for solution of incompressible flow problems. The method blends the generality of the finite-element method with the use of high order polynomial expansions on a nodal grid defined by zeros of certain class of orthogonal polynomials (e.g., Lobatto and Chebyshev polynomials). The discretization is achieved through Galerkin weighted residual projection and integrated using Gaussian quadrature.

There are several applications of time-marching finite-element methods. Initially, time approximation was formulated using Hamilton law of varying action [14]. Later developments showed that weighted residual methods give identical formulations [15]. Bar-Yoseph [16] compared different discretization schemes of the time-marching finite-element method for initial value problems. The author reported the super convergence properties of the discontinuous Galerkin and least square methods over the continuous Galerkin method especially for the element end points [17]. This may yield optimal convergence of the monolithic-time approach; however in this paper we use the last method because of its wide application in the literature. The extension to least squares and discontinuous Galerkin is reserved for later investigations.

Within the context of space–time finite-elements, there have been many time-marching formulations based on least squares [18–21], discontinuous Galerkin method [22–28]. (This is not meant to be an exhaustive list; the interested reader may refer to the reference lists of the above papers for a thorough review of these methods). In the least squares method the authors [18–21] applied a coupled space–time discretization to the solution of incompressible Navier–Stokes equations. The first reference used a variational space–time formulation which enables computation of the deformation of the spatial domain with respect to time. In all the references the time interval was divided into small time strips. In each time strip, an initial boundary value problem was solved and the solution is time-marched to steady-state. A time-marching scheme similar to one used by Tezduyar et al. [18] but with a discontinuous Galerkin discretization have also been applied for a space–time formulation [22–24]. The method was applied to the solution of compressible Navier–Stokes equations [22] and Euler equations of gas dynamics [24]. The space–time elements are constructed by connecting spatial elements between two closely spaced time levels using linear interpolation in time [22]. However, in contrast to the monolithic-time approach, the long-time solution is computed in numerous time steps.

On the other hand examples of finite-difference time-marching schemes constitute the overwhelming majority of numerical integration algorithms. Some examples include explicit Runge–Kutta [29] methods and the widely adopted implicit Newmark scheme [30,31]. Development of these schemes to compute the time-dependent solution of Euler and Navier–Stokes equations [32–35] is still attracting considerable attention.

A computational efficiency can be achieved when the finite-difference or finite-element methods in time are formulated to take advantage of systems with periodic responses. Here the time dimension is reduced into a single period and minimal number of degrees-of-freedom (DOFs) are needed to approximate the solution. The analysis of periodic solutions using finite-difference methods was implemented by Doedel [36], Holodniok and Kubicek [37] using continuation methods. These algorithms still attract attention in different applications [38,39]. Other methods use inherently periodic functions such as Fourier methods [40], dubbed in the literature as the Harmonic Balance method (HB) [41–43]. In this method, the inherent periodicity of the Fourier expansion proved efficient in handling periodic responses inherent to turbomachinery and aeroelastic applications. In contrast to SE, the Fourier coefficients are applied globally over the entire time domain. This global property of the Fourier coefficients introduces a weakness in handling excitations with many frequencies. To provide a more local control, Gopinath et al. [44] applied the SE method to periodic solutions using the cyclic method with equal-element spacing. The method compared favorably with the time-spectral (HB) method and finite-difference scheme for the computation of limit-cycle oscillations. In a recent application Schilder et al. [45] developed a new Fourier method that combines HB and averaging method to handle quasi-periodic oscillations.

In this paper, we consider both periodic and transient solutions of differential equations that are rapidly excited. For periodic problems, periodicity of the array of spectral elements is physically enforced over a single cycle. In contrast, the transient solution is computed from the initial conditions up to a monolithic-time interval that include the converged dynamics. In both cases, the solution is obtained in one non-iterative calculation for linear problems. Additionally, we use element clustering near the rapid time transients to maintain the efficiency and accuracy of the method without increase in DOFs.

Section 2 continues with description of a standard form of differential equations, followed by the monolithic-time discretization using spectral elements. Section 3 provides results of case studies derived from several applications, Section 4 reports on numerical issues and Section 5 summarizes the main conclusions of the paper.

2. Analysis

In this section, we introduce, and restrict attention to, a standard form of a set of first-order linear differential equations. Next, the spectral element method is used to discretize the time-derivative operator for transient and steady-state/periodic solutions.

2.1. Standard form

The spectral element method is applied to a particular set of linear first-order differential equations that we call here as *standard form*: The coupled set of differential equations has one in front of the unsteady term,

$$\frac{\mathrm{d}x}{\mathrm{d}t} + \mathbf{A}_s x = f(t), \tag{2.1}$$

where x represents the collocated dependent variables $x \in R^{N_v}$, N_v is the number of dependent variables, time t is the independent variable, and $f(t)$ is assumed to be a known function of time. The equations are coupled through the matrix $\mathbf{A}_s$, which is assumed to be time invariant. Eq. (2.1) can be contrasted with a more general form that admits higher order unsteady terms, although we attempt to tackle higher order unsteady terms by transforming to the first-order form.

Ordinarily, initial conditions need to be specified in simulating (2.1). However, this is generally not the case when cyclic solutions of (2.1) are sought, i.e., those that are time-periodic in response to a time-periodic

forcing function, $f(t)$, with a circular frequency, ω. For example, consider (2.1) to be a scalar equation of the form ($a > 0$),

$$\frac{\mathrm{d}x}{\mathrm{d}t} + ax = f(t) = b\sin\omega t, \tag{2.2}$$

along with the initial condition $x(0) = x_0$. Using an integrating factor, the general solution is expressed as

$$x(t) = \exp(-at)\left[x_0 + \int_0^t b\exp as\sin\omega s\,\mathrm{d}s\right], \tag{2.3a}$$

$$x(t) = \exp(-at)\left[x_0 + \frac{b\exp(at)(a\sin\omega t - \omega\cos\omega t)}{a^2+\omega^2} + \frac{b\omega}{a^2+\omega^2}\right], \tag{2.3b}$$

$$x(t) \approx \frac{b}{a^2+\omega^2}[a\sin\omega t - \omega\cos\omega t], \quad (\text{as } t\to\infty). \tag{2.3c}$$

Note that the long-time solution given in (2.3c) requires no initial condition; specification of $f(t)$ is sufficient to obtain the relative amplitude and phase of the resulting solution. The details ensuing shortly after the initial condition do not impact long-term behavior. An exception occurs at $a = 0$ when $\exp(at)$ no longer is large and x_0 cannot be neglected. Furthermore, when $a < 0$, the homogeneous solution is divergent; we shall not consider this case.

2.2. Spectral element time discretization

In this section we describe the time discretization of transient and periodic responses for one dependent variable using a spectral element (SE) formulation, and then describe the global assembly for many dependent variables.

2.2.1. Transient analysis

Each dependent variable can be discretized in time using spectral elements [46], where the approximate mth order solution in each element is:

$$\hat{x}^{(j)}(\zeta) = \sum_{k=0}^{m} x^{(j)}(\zeta_k)\psi_k^{(j)}(\zeta). \tag{2.4}$$

Here $\hat{x}^{(j)}(\zeta)$ is the approximate solution, $\psi_k^{(j)}$ represents the Lagrange polynomial of order k in element j, $x^{(j)}(\zeta_k)$ are the unknown nodal values placed at ζ_k for element j and ζ_k are the Legendre–Lobatto points placed at zeros of the completed Lobatto polynomials defined on the interval $\zeta \in [-1,1]$ according to [47, p. 143]

$$L^c_{o_{m+1}}(\zeta) = (1-\zeta^2)L_{o_{m-1}}(\zeta). \tag{2.5}$$

The domain is depicted in Fig. 2.1, where the physical time domain $t \in [t_j, t_{j+1}]$ is transformed to the ζ domain for each element. The Lobatto polynomials L_{o_i} are a set of orthogonal polynomials that can be defined as the derivatives of the Legendre polynomials [47], L_i:

$$L_{o_i}(\zeta) \equiv L'_{i+1}(\zeta), \tag{2.6}$$

where the Legendre polynomials are defined explicitly as

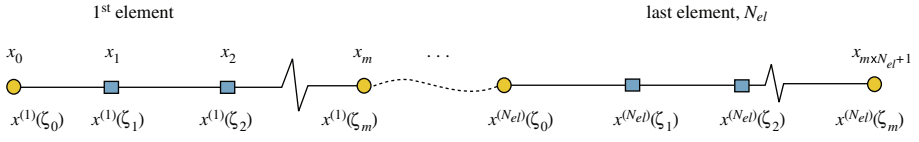

Fig. 2.1. Discretization of the time domain into N_{el} elements represented by an m order Lagrange polynomial within each element. Nodes of each element are placed at zeros of completed Lobatto polynomials.

$$L_i(\zeta) = \frac{1}{2^i i!}\frac{\mathrm{d}^i(\zeta^2-1)^i}{\mathrm{d}\zeta^i}. \tag{2.7}$$

We review the development of SE here for completeness. Substituting the trial solution (2.4) into the differential equation (2.1) and minimizing the residual using the Bubnov–Galerkin method [48] we have (assume A_s is scalar for now):

$$\sum_{j=1}^{N_{el}}\int_{-1}^{1} v(\zeta)\left[\frac{\mathrm{d}\hat{x}^{(j)}}{\mathrm{d}\zeta}+\frac{h^{(j)}}{2}\left\{A_s\hat{x}^{(j)}-f^{(j)}(\zeta)\right\}\right]\mathrm{d}\zeta = 0, \tag{2.8}$$

where $h^{(j)}$ is the width of element j and $v(\zeta)$ is a weighting function taken as the pth order Lagrange polynomial, $\psi_p^{(j)}$. Integrating by parts we find for $p = 0,\ldots,m$:

$$\sum_{j=1}^{N_{el}}\left[\hat{x}^{(j)}\psi_p^{(j)}|_{-1}^{1}-\int_{-1}^{1}\left(\hat{x}^{(j)}\frac{\mathrm{d}\psi_p^{(j)}}{\mathrm{d}\zeta}-\frac{h^{(j)}}{2}\{A_s\hat{x}^{(j)}\psi_p^{(j)}-f^{(j)}(\zeta)\psi_p^{(j)}\}\right)\mathrm{d}\zeta\right] = 0. \tag{2.9}$$

Exploiting the property of Lagrange polynomials, (2.9) is efficiently integrated using Gauss–Lobatto Legendre quadrature rule which includes the end points

$$\int_{-1}^{1} Q\mathrm{d}\zeta = \sum_{q=0}^{m} Q(\zeta_q)\omega_q, \tag{2.10}$$

where Q is a generic function of ζ and ω_q is the Gaussian quadrature weight at node q. This gives the following compact matrix formulation for each element:

$$\mathbf{\Psi}\begin{Bmatrix} x(\zeta_0)\\ \vdots\\ x(\zeta_m)\end{Bmatrix}^{(j)} = A_s\mathbf{I}_\omega^{(j)}\begin{Bmatrix} x(\zeta_0)\\ \vdots\\ x(\zeta_m)\end{Bmatrix}^{(j)} - \mathbf{I}_\omega^{(j)}\begin{Bmatrix} f(\zeta_0)\\ \vdots\\ f(\zeta_m)\end{Bmatrix}^{(j)}, \tag{2.11}$$

where

$$\mathbf{\Psi} = \begin{bmatrix} \left(\frac{\mathrm{d}\psi_0}{\mathrm{d}\zeta}|_{\zeta_0}\omega_0+1\right) & \frac{\mathrm{d}\psi_0}{\mathrm{d}\zeta}|_{\zeta_1}\omega_1 & \cdots & \frac{\mathrm{d}\psi_0}{\mathrm{d}\zeta}|_{\zeta_m}\omega_m\\ \frac{\mathrm{d}\psi_1}{\mathrm{d}\zeta}|_{\zeta_0}\omega_0 & \frac{\mathrm{d}\psi_1}{\mathrm{d}\zeta}|_{\zeta_1}\omega_1 & \cdots & \vdots\\ \vdots & \cdots & \cdots & \frac{\mathrm{d}\psi_{m-1}}{\mathrm{d}\zeta}|_{\zeta_m}\omega_m\\ \frac{\mathrm{d}\psi_m}{\mathrm{d}\zeta}|_{\zeta_0}\omega_0 & \cdots & \frac{\mathrm{d}\psi_m}{\mathrm{d}\zeta}|_{\zeta_{m-1}}\omega_{m-1} & \left(\frac{\mathrm{d}\psi_m}{\mathrm{d}\zeta}|_{\zeta_m}\omega_m-1\right)\end{bmatrix}, \tag{2.12}$$

and

$$\mathbf{I}_\omega = \frac{h^{(j)}}{2}\begin{bmatrix}\omega_0 & 0 & \ldots & 0\\ 0 & \omega_1 & \ldots & 0\\ \vdots & \vdots & \ddots & \vdots\\ 0 & 0 & \ldots & \omega_m\end{bmatrix}. \tag{2.13}$$

In (2.12), the first and last diagonal elements of differentiation matrix $\mathbf{\Psi}$ have an additional term (=1) due to the first term in (2.9). The essential inter-element continuity between subsequent elements

$$x^{(j)}(\zeta_m) = x^{(j+1)}(\zeta_0), \tag{2.14}$$

is used to reduce the number of DOFs prior to the assembly of a global system of equations from (2.11) for N_{el} spectral elements. This yields a compact Galerkin projection governing the approximate solution in time (one dependent variable):

$$\mathbf{L}_c X_c = A_s \mathbf{L}_\omega X_c - \mathbf{L}_\omega F. \tag{2.15}$$

where $\mathbf{L}_c$ and $\mathbf{L}_\omega$ are the global differentiation and weight matrices, F is the global weighted form of the excitation and

$$X_c = \left[x|_{t_0} \quad x|_{t_1} \quad \dots \quad x|_{t_{m\times N_{\text{el}}+1}} \right]^{\text{T}}, \tag{2.16}$$

is the SE solution of the dependent variable x collocated at all nodal times (redundant nodes are removed using (2.14)). It should be noted that the initial condition is applied by replacing the first row and column of $\mathbf{L}_c$ with zeros except for the first element, which is replaced with one. Also, the first element in $\mathbf{L}_\omega X_c$ is replaced with zero and the first element in $-\mathbf{L}_\omega F$ is replaced with the value of x at $t = 0$. The SE solution X_c in (2.15) can then be computed using direct or iterative methods.

2.2.2. Periodic cyclic analysis

In some problems, the interest lies in the steady-state time solution, where the response is time-periodic with a period, $T = 2\pi/\omega$, equal to the period of the forcing function. This occurs in damped systems with periodic forcing functions and in self-excited nonlinear systems exhibiting limit-cycle oscillations (LCOs).

In these problems we are interested in the steady-state periodic solution only, where the time cycle is discretized spectrally in the same way as in the transient solution, however, assembly of global matrices $\mathbf{L}_c$ and $\mathbf{L}_\omega$ is different. Here the initial conditions do not affect the long-term periodic solution (see Section 2.1). Additionally, periodicity of the array of elements is enforced by requiring that the end node in the last element to be the initial node of the first element:

$$x^{(1)}(\zeta_0) = x^{(N_{\text{el}})}(\zeta_m). \tag{2.17}$$

Contributions to the end node in the last element are added to contributions from first element. Consequently the last row and column of $\mathbf{L}_c$ are added to their counterpart in the first row and column. Therefore, the solution vector, X_c, becomes

$$X_c = \left[x|_{t_0} \quad x|_{t_1} \quad \dots \quad x|_{t_{m\times N_{\text{el}}}} \right]^{\text{T}}. \tag{2.18}$$

2.3. Global assembly

A number of dependent variables, N_v, can be handled through spatial connectivity matrix $\mathbf{A}_s$ of size $N_v \times N_v$. Here, the tensor product gives the global form of (2.15):

$$(\mathbf{I} \otimes \mathbf{L}_c) X_{cg} = (\mathbf{A}_s \otimes \mathbf{L}_\omega) X_{cg} - (\mathbf{I} \otimes \mathbf{L}_\omega) F_{cg}, \tag{2.19}$$

where $\mathbf{I}$ is the identity matrix of size $N_v \times N_v$ and X_{cg} is a collocation of all dependent variables at nodal times grouped by their corresponding independent variables, N_v. For transient solution X_{cg} takes the form:

$$X_c = \left[\begin{Bmatrix} x_1|_{t_0} \\ x_1|_{t_1} \\ \vdots \\ x_1|_{t_{m\times N_{\text{el}}+1}} \end{Bmatrix}^T \quad \dots \quad \begin{Bmatrix} x_{N_v}|_{t_0} \\ x_{N_v}|_{t_1} \\ \vdots \\ x_{N_v}|_{t_{m\times N_{\text{el}}+1}} \end{Bmatrix}^T \right]^{\text{T}}. \tag{2.20}$$

A compact form of (2.19) becomes

$$\mathbf{L}_{cg} X_{cg} = \mathbf{A}_{cg} X_{cg} - \mathbf{L}_{\omega g} F_{cg}. \tag{2.21}$$

For this linear problem, solution X_{cg} of (2.21) can be computed directly (as opposed to an iterative approach, which would be typically applied for larger systems of practical significance). However, we use Newton's method in anticipation of nonlinear excitations. By identifying a residual R we can write (2.21) as

$$R = \mathbf{L}_{cg} X_{cg} - \mathbf{A}_{cg} X_{cg} + \mathbf{L}_{\omega g} F_{cg}. \tag{2.22}$$

Taylor series expansion of the linear formula (2.22) gives

$$R^{v+1} = R^{v} + \mathbf{J}\Delta X_{cg}, \tag{2.23}$$

where

$$\mathbf{J} = \mathbf{L}_{cg} - \mathbf{A}_{cg}. \tag{2.24}$$

For this linear formulation, the updated residual becomes zero in one iteration. When the formulation is nonlinear (see Section 3.7) additional iterations are required, since (2.23) is an approximation.

3. Case studies

In this section, we apply the spectral element method to three classes of problems. First, we apply the method to a set of linear first-order differential equations that are already in the standard form. Excitations of harmonic and impulsive form are presented. For the latter case we use non-uniform element sizes to handle the impulse excitation. This will demonstrate the method's accuracy and efficiency. Then, we give examples of higher order differential equations that are transformed to the standard form and solved using the SE method in time. The example applications come from heat conduction in one dimension, cantilever beam vibration and the wave equation. Finally, we give an example application of the method to a weak nonlinearity attached to the standard form.

3.1. Standard form: harmonic excitation

3.1.1. Transient analysis

Let us first consider an example according to the standard form in (2.1) with harmonic excitation force, $f(t)$:

$$\frac{\mathrm{d}x}{\mathrm{d}t} + ax = \sin\frac{2\pi t}{T}, \quad 0 \leqslant t \leqslant 10T, \tag{3.1a}$$

$$x(0) = 0, \tag{3.1b}$$

where $a = 1$ and $T = 0.2$ s. Eq. (2.3b) gives the analytical solution, X_a for the transient analysis in the interval $t \in [0,10T]$. The SE solution is reported in the following using equal-sized elements. Here we will compare X_a to the SE solution X_c using the infinity error norm E and energy error norm E_2. The error norms are evaluated for different combinations of number of elements, N_{el}, and Lagrange polynomial order, m. In Fig. 3.1a, E is

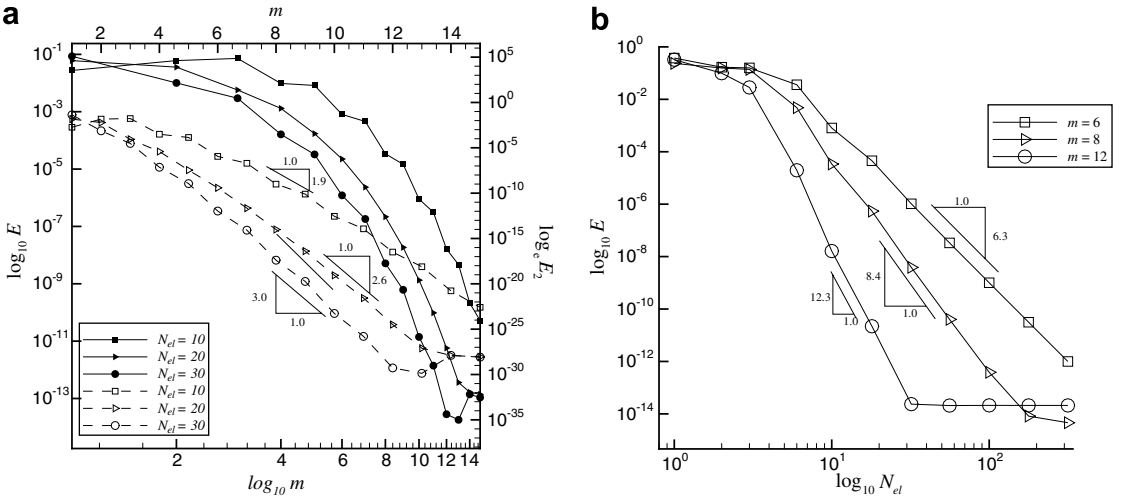

Fig. 3.1. Transient analysis of linear system with harmonic excitation (a) E versus $\log_{10}(m)$ – solid lines and filled symbols and $\log_e(E_2)$ versus m – dashed lines and hollow symbols and (b) error norm as a function of number of elements, N_{el}.

reported as a function of m for three different values of N_{el}, where the filled symbols denote the relationship. As indicated in the figure, E reaches an accuracy of 10^{-11} with $\{N_{el}, m\} = \{20, 12\}$ (240 DOFs). Extensions in element size and polynomial order give an exponential rate of reduction in the energy norm of the error according to [49, p. 66]

$$E_2 \leqslant \frac{k}{\exp(\beta \mathrm{DOF}^{\gamma})}, \tag{3.2}$$

where k, β and γ are positive constants. Under certain conditions Szabo and Babuska [49] report $\gamma = 1/2$. For a constant number of elements (3.2) can be written as

$$E_2 \leqslant \frac{k_m}{\exp(\beta_m m^{\gamma})}, \tag{3.3}$$

For a $\gamma = 1$, Fig. 3.4a reports the E_2 error norm as a function of m. The figure indicates the rates of convergence for the constant $-\beta_m$. This validates the exponential convergence rate of SE method for all nodal times. Fig. 3.4b, reports similar data, but as a function of N_{el} for different values of m. Here a constant polynomial convergence is observed. For example, $m = 6$ gives approximately N^{-6} convergence rate. In both figures, we note that the convergence rate deteriorates when E reaches machine accuracy, this is due to the limitation in number of significant figures used in the calculations. Using $\{N_{el}, m\} = \{30, 11\}$ we report the SE solution X_c for $t \in [0, 10T]$ in Fig. 3.2, where we note the solution includes both transient and steady-state responses.

3.1.2. Cyclic analysis

In many cases, we are interested in the steady-state solution left after the transient solution dies out. Periodic excitations can give rise to periodic and non-periodic steady-state responses. This is the case for nonlinear systems and even in undamped linear systems. However, here we focus on systems exhibiting periodic steady-state response, in particular (2.1). In this case, (2.1) can be cast in a cyclic form:

$$\frac{\mathrm{d}x}{\mathrm{d}s} + aTx = T \sin 2\pi s, \quad 0 \leqslant s \leqslant 1, \tag{3.4}$$

where the time is normalized by the period T to give a scaled time over the cycle, $s = t/T$. Cyclic analysis of (3.4) is compared to the long-time solution provided in (2.3c).

The cyclic SE solution is calculated over one cycle without the need to time-march through the transients. This results in a smaller number of DOFs needed to attain high accuracy. For example, for a period of $T = 0.2$ and $a = 1$ as before, the computed cyclic solution is shown in Fig. 3.3, where the gap in the orbit is a result of enforcing the time-periodic boundary condition. However, the SE solution is valid for an arbitrary $t \in [0, T]$ through the chosen high order polynomial basis.

The error norm, E, is calculated in Fig. 3.4a for fixed N_{el} and increasing m. In the figure we observe the previously noted exponential convergence. In Fig. 3.4b E is computed for constant m and increasing order

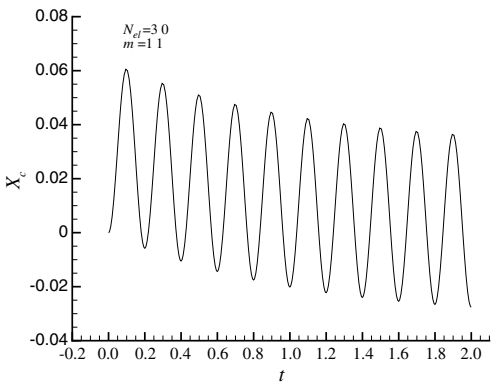

Fig. 3.2. SE transient solution for harmonic forcing function of (3.2).

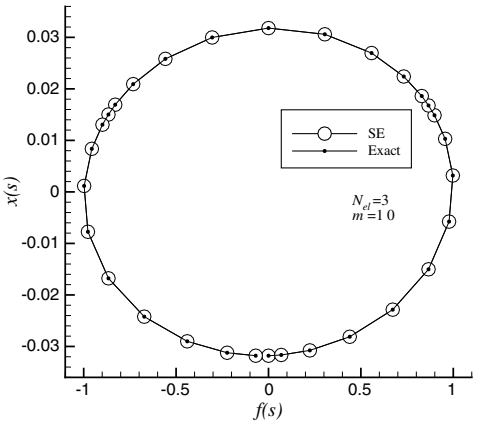

Fig. 3.3. Periodic orbit of harmonic forcing function and cyclic response for one dependent variable, X_c.

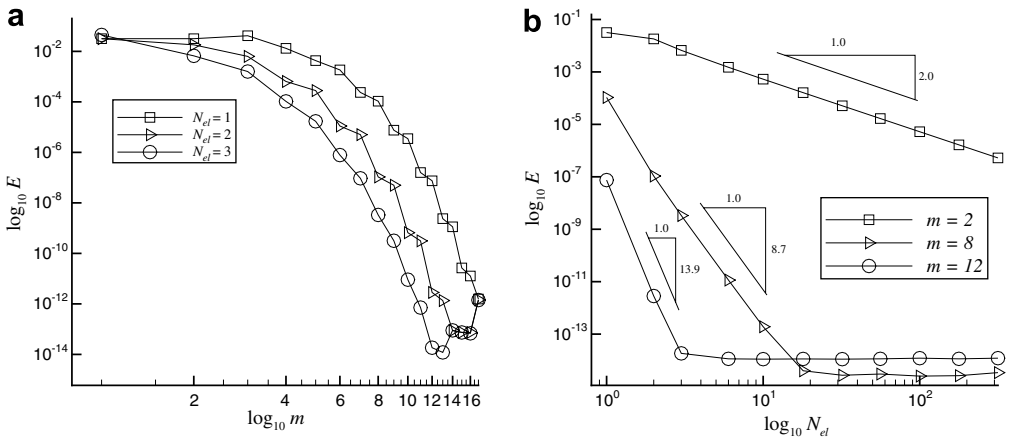

Fig. 3.4. Cyclic analysis of linear system with harmonic excitation: (a) error norm as a function of polynomial order, m; (b) error norm as a function of number of elements, N_{el}.

N_{el}. Because the solution is computed over one cycle, only 24 DOFs ($m = 12, N_{\mathrm{el}} = 2$) are needed here to achieve 10^{-11} accuracy.

3.2. Standard form: impulsive excitation – transient analysis

In an abrupt variation of the excitation, the high convergence rate of the SE method can not be maintained using fixed-size elements. An impulsive excitation is an example of such variation: see Fig. 3.5a. After including a mathematical representation of such impulsive excitation, the standard form becomes

$$\frac{\mathrm{d}x}{\mathrm{d}t} + 0.6x = 10\exp\frac{-(t-0.5)^2}{\epsilon}, \quad 0 \leqslant t \leqslant 1, \tag{3.5a}$$

$$x(0) = 0.5, \tag{3.5b}$$

where the sharpness of the impulse located at $t = 0.5$, see Fig. 3.5a, can be controlled by adjusting the value of ϵ. Although we considered different values of ϵ we report results for $\epsilon = 1.125 \times 10^{-4}$. The analytical solution for this differential equation is found using the integrating factor approach and integrated with Mathematica®:

$$x = \exp(-0.6t)[A_1 \mathrm{erf}(A_2 - A_3 t) + A_4], \tag{3.6}$$

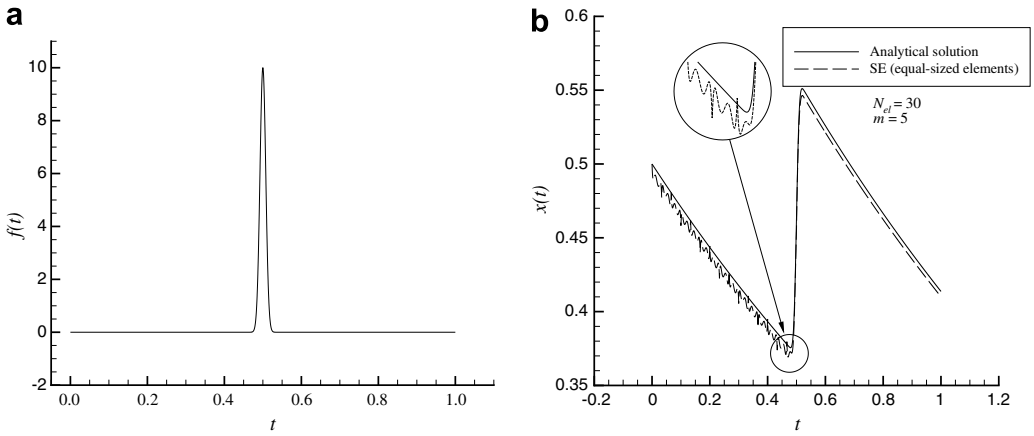

Fig. 3.5. (a) An impulse excitation force and (b) SE solution X_c using equal-sized elements, where numerical inaccuracies are observed in the computation of X_c.

where

$$A_1 = -0.12688606923349941,$$
$$A_2 = 47.1436340596185,$$
$$A_3 = 94.28090415820633,$$
$$A_4 = 0.62688606923349941,$$
$$\operatorname{erf} z = \frac{2}{\sqrt{\pi}} \int_0^z \exp(-w^2)\,\mathrm{d}w.$$

The solution X_c is first computed using equal-sized elements. Fig. 3.5a shows the numerical "noise" (due to under-resolution) resulting from the rapid variation in the actuation. To circumvent this difficulty, the elements are clustered near this rapid variation without increasing the total number of elements or interpolation nodes. The degree of clustering is shown in Fig. 3.6a. To refine the elements, the element sizes are increased or decreased in a geometric fashion. This variation is controlled using specific ratio, r, for which the ratio of the first element and the element near the rapid variation, N^*: have a specific value:

$$r = \frac{h^{(N^*)}}{h^{(1)}}. \tag{3.7}$$

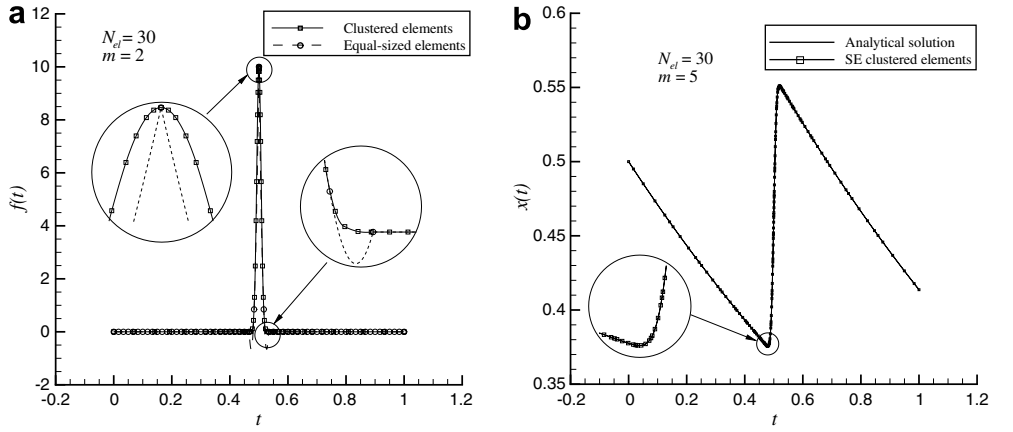

Fig. 3.6. (a) Representation of impulsive excitation using equal-sized and clustered elements and (b) SE solution X_c using clustered elements.

In Fig. 3.6b, the elements are clustered near the abrupt variation at $t = 0.5$ using $r = 0.01$, where the value of r is selected to resolve the rapid excitation instituted by the value of ϵ. Although the same number of DOFs were used ($N_{\text{el}} = 30$ and $m = 5$) in the equal-sized and clustered elements cases, we observe in the figure that, element clustering has eliminated the numerical inaccuracies in the solution.

The superiority of element clustering is even more apparent in Fig. 3.7a. The figure shows that using the element clustering approach gives better accuracy than equal-sized elements, even with smaller number of DOFs. The former gives a combination of $\{E, \text{DOFs}\}$ of $\{10^{-13}, 400\}$ opposed to $\{10^{-11}, 720\}$ for equal-sized elements. In Fig. 3.7b the error is computed for equal-sized elements with increasing order m and compared to element clustering with low order m. The figure emphasizes that equal-sized elements with any m can not out perform the element clustering case.

3.3. Mass–spring–damper system: harmonic excitation

A typical example of a second-order differential equation is the mass–spring–damper system:

$$m\ddot{x} + c\dot{x} + kx = b\sin\omega t, \qquad 0 \leqslant t \leqslant t_e, \tag{3.8}$$

with initial conditions,

$$x(0) = x_0,$$
$$\dot{x}(0) = v_0.$$

The analytical solution of (3.8) for an underdamped $c^2 < 4mk$ system can be found in many textbooks (see, for example, Steidel [50]):

$$x = \exp\left(-\frac{c}{2m}t\right)\left[(x_0 - C)\cos\omega_d t + \frac{v_0 - D\omega + \frac{c(x_0 - C)}{2m}}{\omega_d}\sin\omega_d t\right] + C\cos\omega t + D\sin\omega t, \tag{3.9}$$

where

$$C = -\frac{bc\omega}{m^2\left[(\omega_n^2 - \omega^2)^2 + \left(\frac{c\omega}{m}\right)^2\right]},$$
$$D = \frac{b(\omega_n^2 - \omega^2)}{m[(\omega_n^2 - \omega^2)^2 + \left(\frac{c\omega}{m}\right)^2]},$$

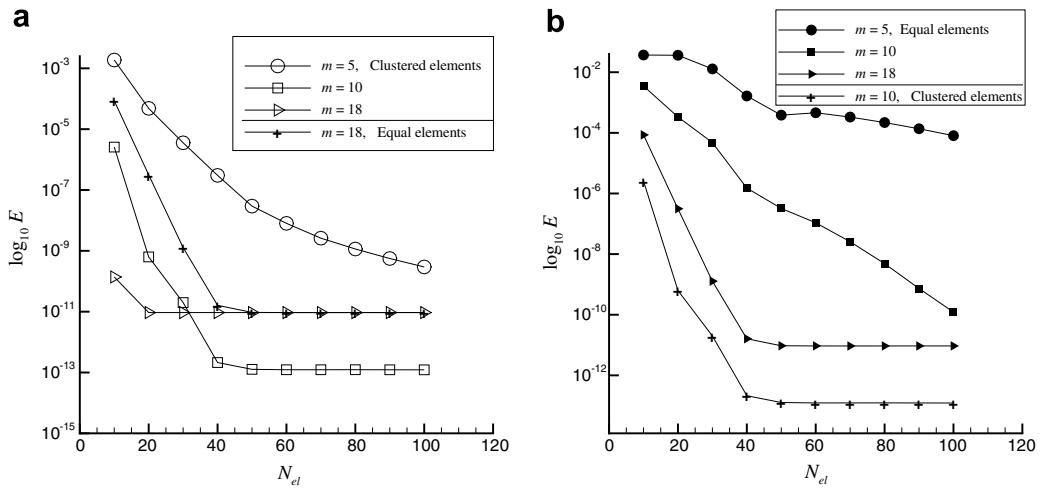

Fig. 3.7. Transient analysis of impulsive excitation. Effect of element clustering on the error norm. (a) Cases of clustered elements compared to a high order equal-sized element case and (b) cases of equal-sized elements compared to a clustered element case.

Table 1
Parameters used in mass–spring–damper problem

m	c	k	b	x_0	v_0	T	t_e
1	0.3	20	2000	10	20	0.2	$200T$

where ω_d is the damped natural frequency. The first two terms in (3.9) contains the initial conditions. This is the transient solution, whereas the last two terms constitute the time-periodic solution. In the following, we solve the equation using transient and cyclic analysis for the parameters listed in Table (1).

3.3.1. Transient analysis

In order to solve (3.8) using the SE method, the equation is transformed to the standard form by introducing two variables $x_1 = \dot{x}$ and $x_2 = x$:

$$\begin{Bmatrix} \dot{x_1} \\ \dot{x_2} \end{Bmatrix} + \begin{bmatrix} m & 0 \\ 0 & 1 \end{bmatrix}^{-1} \begin{bmatrix} c & k \\ -1 & 0 \end{bmatrix} \begin{Bmatrix} x_1 \\ x_2 \end{Bmatrix} = \begin{bmatrix} m & 0 \\ 0 & 1 \end{bmatrix}^{-1} \begin{Bmatrix} b \sin \omega t \\ 0 \end{Bmatrix}. \tag{3.10}$$

The matrix product in front of the vector $[x_1, x_2]^{\mathrm{T}}$ represents a coupled form of the matrix $\mathbf{A}_s$. In Fig. 3.8a, the SE solution of (3.10) is computed and compared to the analytical solution. We note that the periodic solution of this lightly damped system needed to evolve through $150T$ periods to mature to near steady-state. This required the large value of N_{el} used here, where an approximately one element is used per oscillation. This large number of elements explains the degradation in the displacement error norm, E reported in Fig. 3.8b, where the error continues to decrease exponentially up to a refinement stage beyond which an increase in the polynomial order or number of elements becomes unfavorable. This is mainly due to machine precision limitations, in which the round-off error starts to dominate the total error.

3.3.2. Cyclic analysis

Following Section 3.1.2, the time-periodic solution of (3.8) can be computed by transforming the second-order differential equation into cyclic form, where the physical time t is scaled by the period T, to get a scaled time s. The equation can then be cast in standard form:

$$\frac{1}{T^2} \begin{Bmatrix} \dot{x_1} \\ \dot{x_2} \end{Bmatrix} + \begin{bmatrix} m & 0 \\ 0 & 1 \end{bmatrix}^{-1} \begin{bmatrix} \frac{c}{T} & k \\ -\frac{1}{T^2} & 0 \end{bmatrix} \begin{Bmatrix} x_1 \\ x_2 \end{Bmatrix} = \begin{bmatrix} m & 0 \\ 0 & 1 \end{bmatrix}^{-1} \begin{Bmatrix} b \sin 2\pi s \\ 0 \end{Bmatrix} \tag{3.11}$$

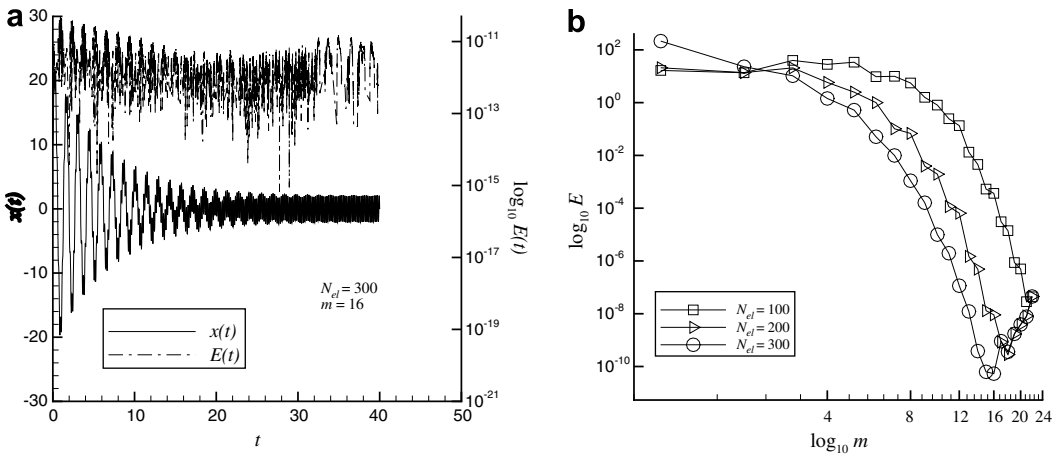

Fig. 3.8. Transient analysis of mass–spring–damper system. (a) SE solution compared to analytical solution and (b) displacement error norm.

Additionally, the cyclic analytical solution can be reduced from (3.9) by retaining the long-time solution ($t \to \infty$) and then transforming t to scaled time s:

$$x = C\cos 2\pi s + D\sin 2\pi s \tag{3.12}$$

The cyclic/SE solution of (3.11) is computed in Fig. 3.9a and compared to the analytical solution in (3.12). From the figure, we observe the close agreement between both and for a relatively small number DOFs compared to the transient analysis. When only the steady-state solution is of interest, the cyclic analysis provides the means for an efficient and accurate integration.

The advantage of using cyclic analysis is more apparent in Fig. 3.9b, where in contrast to transient analysis, only small number of DOFs are needed to achieve high accuracy. Consequently, the error norm continued to decrease exponentially with minimal degradation in accuracy due to the extra refinement.

3.4. Cantilever beam vibration: harmonic excitation

The vibration of a cantilever beam serves as a model to many engineering applications. See for example a recent application in micro-air vehicles [51], where periodic resonant vibrations of the wing are used to power the vehicle into flight. The wing in this case can be modeled as a nonlinear beam with the desire to compute time-accurate response of the beam flapping motion. The partial differential equation governing the flexure vibration of a cantilever beam (e.g., [52]) is of fourth-order in the spatial dimension. The differential equation can be discretized spatially using the conventional finite-element method (3D beam elements) to lead to a set of second-order differential equations with t as the independent time variable [53,54]:

$$\mathbf{M}\{\ddot{w}\} + \mathbf{K}\{w\} = f(t), \tag{3.13}$$

where

$$\dot{w}(0) = 0 \qquad w(0) = 0,$$

where $\{w\}$ is a collocation of the nodal deflections. Each node consists of 6 deflections with 3 displacements $\{x, y, z\}$ and 3 rotations $\{\theta_x, \theta_y, \theta_z\}$. Note that we leave out the structural damping here. This will allow us to study effectiveness of the cyclic SE method in handling quasi-periodic responses.

We consider a beam of the geometry described in Table (2), where E_{Young} is Young modulus of elasticity, G is shear modulus of elasticity, I_y is the cross-sectional area moment of inertia about the axis normal to x and z, see Fig. 3.10, similarly I_z but about the axis normal to x and y, ρ is the beam density, L is the beam length, A is the beam area and b is the harmonic force amplitude.

The beam is discretized spatially using general Euler beam elements, with 6 DOFs per node. MSC.Nastran [55] is used in generating **M** and **K** square matrices. We use 10 elements to discretize the beam into 11 nodes (66 DOFs total).

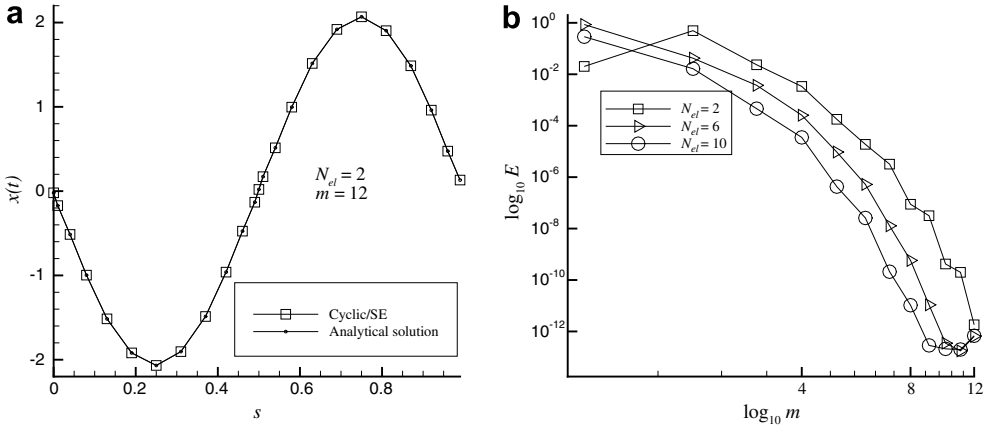

Fig. 3.9. Cyclic analysis of mass–spring–damper system. (a) SE solution computed over a cycle compared to analytical solution and (b) error norm.

Table 2
Cantilever beam problem characteristics and loading amplitude

I_z, in.^{4}	I_y, in.^{4}	E_{Young}, psi	G, psi
1450	1296	10×10^6	3.9×10^6
A, in.^{2}	L, in	ρ, lbf s^2/in.^{4}	b, lbf
19.5	100	2.588×10^{-4}	30×10^3

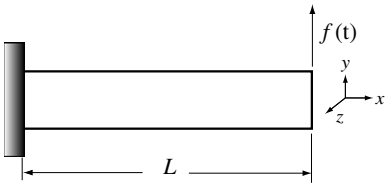

Fig. 3.10. Cantilever beam schematic

In the following, we use the SE method to compute the transient and cyclic response for (3.13) with a periodic force $f(t) = b\sin\omega t$ acting at the beam tip in the y direction.

3.4.1. Transient analysis

To solve (3.13) using the SE method, we write the second-order equation in first-order form, where $x_1 = \dot{w}$ and $x_2 = w$ are collocation of nodal velocities and displacements, respectively, along the beam:

$$\begin{Bmatrix} \dot{x}_1 \\ \dot{x}_2 \end{Bmatrix} + \begin{bmatrix} \mathbf{M} & \mathbf{0} \\ \mathbf{0} & \mathbf{I} \end{bmatrix}^{-1} \begin{bmatrix} \mathbf{0} & \mathbf{K} \\ -\mathbf{I} & \mathbf{0} \end{bmatrix} \begin{Bmatrix} x_1 \\ x_2 \end{Bmatrix} = \begin{bmatrix} \mathbf{M} & 0 \\ \mathbf{0} & \mathbf{I} \end{bmatrix}^{-1} \{f(t)\}, \qquad \{x_1(0)\} = \{0\} \quad \{x_2(0)\} = \{0\}, \tag{3.14}$$

where

$$\{f(t)\} = [\,[0\ldots0\ b\sin\omega t\ 0\ 0\ 0\ 0][0\ldots0]\quad]^{\mathrm{T}}.$$

The solution of (3.14) is computed first for a forcing frequency of 5 Hz ($\omega = 10\pi$), which is far from the fundamental frequency, f_n, of the beam (95 Hz). Fig. 3.11a gives the SE solution X_c compared to solutions computed using MSC.Nastran. The latter uses a coupled mass matrix and a central-difference integration scheme similar to Newmark-Beta direct integration scheme. The solution is computed for a time interval up to $t = 5T$ with $N_{\text{el}} = 100$ and $m = 10$. In the figure, we see excellent agreement between the two methods.

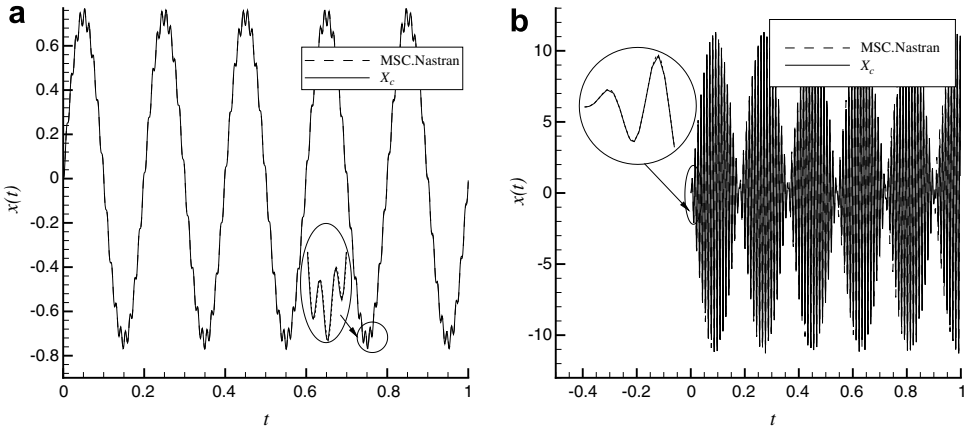

Fig. 3.11. Transient analysis of cantilever beam. (a) Tip-displacement of beam for a harmonic excitation of $\omega = 10\pi$. (b) Tip-displacement of beam for a harmonic excitation of $T = 1/f_n$.

Exciting the beam near its fundamental frequency gives a different response. Here the vibration amplitude of the beam at its fundamental frequency is comparable to the primary forced vibrations. The SE solution is computed up to $t = 1$ s. Again we see in Fig. 3.11b good agreement with the MSC. Nastran solution.

3.4.2. Cyclic analysis

The cyclic form of (3.14) is

$$\frac{1}{T^2}\begin{Bmatrix}\dot{x}_1\\ \dot{x}_2\end{Bmatrix} + \begin{bmatrix}\mathbf{M} & \mathbf{0}\\ \mathbf{0} & \mathbf{I}\end{bmatrix}^{-1}\begin{bmatrix}\mathbf{0} & \mathbf{K}\\ -\frac{1}{T^2}\mathbf{I} & \mathbf{0}\end{bmatrix}\begin{Bmatrix}x_1\\ x_2\end{Bmatrix} = \begin{bmatrix}\mathbf{M} & \mathbf{0}\\ \mathbf{0} & \mathbf{I}\end{bmatrix}^{-1}\{f(s)\}, \tag{3.15}$$

where

$$\{f(s)\} = [\,[0\ldots0\ b\sin 2\pi s\ 0\ 0\ 0\ 0] \quad [0\ldots0]\,]^{\mathrm{T}}.$$

Although the response of the undamped cantilever beam is periodic, its frequency content consists of the beam fundamental frequency and the forcing frequency. When the forcing frequency (5 Hz) is far from the natural frequency, the resonance of the beam is minimal and the response is approximately periodic at the forcing frequency. For this case, the periodic solution of (3.15) can be computed using the cyclic/SE method. In Fig. 3.12, the cyclic response is computed using $N_{\mathrm{el}} = 2$ and $m = 12$. This is compared to the transient response for one cycle of $0 \leqslant t \leqslant 0.2$, where $N_{\mathrm{el}} = 10$ and $m = 10$ were used to capture the multi-frequency content of the transients. The figure shows that the cyclic solution approximates the amplitude and phase of the transient response reasonably well.

Note that when damping is present, the transient vibrations at the natural frequency will eventually cease and the cyclic solution will give exactly the steady-state periodic response. This was shown in Section 3.3.2.

3.5. One-dimensional diffusion equation

The one-dimensional diffusion equation is a parabolic partial differential equation; it can describe many diffusion processes. We consider here heat conduction in a rod subject to time-periodic variation of the temperature at the left side, constant temperature at the right side and zero initial temperature everywhere along the rod:

$$\frac{\partial u}{\partial t} = \alpha^2\frac{\partial^2 u}{\partial z^2}, \tag{3.16}$$

$$u(0,t) = f(t) = \begin{cases} Q & \text{if } 0 \leqslant t \leqslant T/2;\\ -Q & \text{if } T/2 < t < T.\end{cases}$$

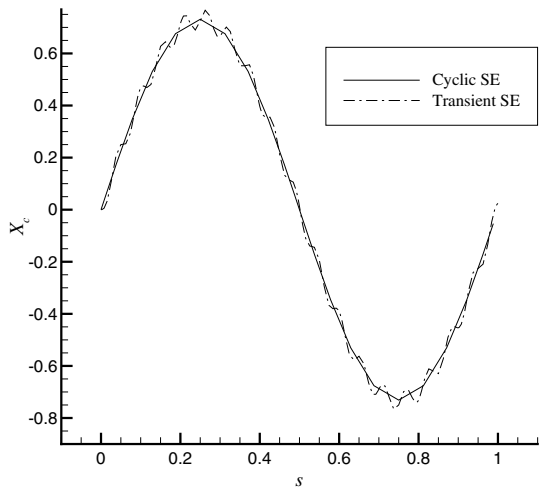

Fig. 3.12. Steady-state tip-displacement of beam.

$$u(L,t)=0,$$
$$u(z,0^{-})=0,$$

where the rod longitudinal axis is in the z direction, α^2 is the thermal conductivity and the time-periodic excitation is a square wave with an amplitude of Q and period T.

Eq. (3.16) can be placed in standard form (2.1). To facilitate this transformation, the rod is divided into n nodes ($n-1$ spatial intervals), with a uniform interval size of $h=1/(n-1)$. The spatial derivatives are approximated using second-order-accurate central finite-difference for the interior nodes and forward and backward finite-differences for the side nodes. The finite-difference approximation of the spatial derivatives become

$$\mathbf{A}^{*}=\alpha^2\frac{\delta^2}{\delta z^2}(\cdot)=\frac{\alpha^2}{h^2}\begin{bmatrix}1&-2&1&0&0&\dots&0\\1&-2&1&0&0&\dots&0\\0&1&-2&1&0&\dots&0\\\vdots&\ddots&\ddots&\ddots&\ddots&\ddots&\vdots\\0&\dots&0&1&-2&1&0\\0&0&\dots&0&1&-2&1\\0&\dots&\dots&0&1&-2&1\end{bmatrix}. \tag{3.17}$$

Note that singularity of matrix $\mathbf{A}^{*}$ is removed after applying the boundary conditions, where the first and last {row,column} of $\mathbf{A}^{*}$ are deleted to get the matrix $\mathbf{A}_s$. The first-order form of (3.16) becomes

$$\begin{Bmatrix}\dot{u}_2\\\vdots\\\dot{u}_{n-1}\end{Bmatrix}+\mathbf{A}_s\begin{Bmatrix}u_2\\\vdots\\u_{n-1}\end{Bmatrix}=\begin{Bmatrix}-A^{*}_{(2,1)}f(t)\\0\\\vdots\\0\end{Bmatrix}. \tag{3.18}$$

Note that the number of elements on the right hand side of (3.18) is $n-2$. In the following we compute the SE transient and cyclic solutions of (3.18), with the boundary temperature fluctuations having a period of $T=0.05$ and for $\alpha^2=0.86$ (the thermal conductivity of Aluminum). The rod is divided spatially into $n=100$ nodes.

3.5.1. Transient analysis

The transient solution is computed in Fig. 3.13 for a time interval up to $30T$. Fig. 3.13a gives the temperature solution at node $n=2$ (node next to the fluctuating boundary). In order to cope with the rapid (in this case, discontinuous) variation in the forcing function $f(t)$ we use a somewhat high $N_{el}=1000$ and $m=10$. The

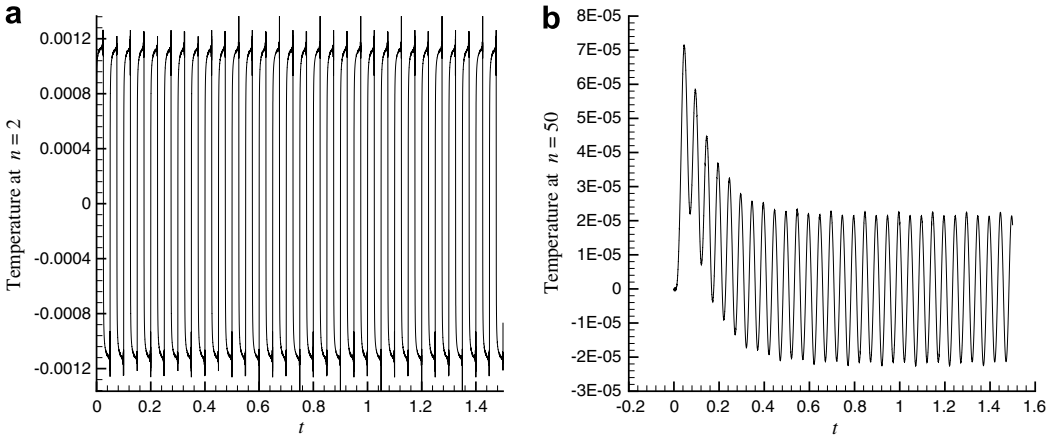

Fig. 3.13. Transient solution computed for a forcing period, $T=0.05$.

effect of the periodic rapid excitation should diminish as we move away from the left node. Because $n = 2$ is close to the time-periodic boundary condition, strong periodicity of the solution is observed. However, due to the rapid variation in each time-period numerical errors are observed in the solution. The temperature response is reported in Fig. 3.13b for node $n = 50$ corresponding to mid of the rod. The response is observed to settle into periodic oscillations at long-time ($t = 12T$). A phase plot of the last cycle in the transient response ($29T$), see Fig. 3.14a, for nodes $n = 2$ and $n = 50$ illustrate the numerical "noise" observed in Fig. 3.13a for node $n = 2$. Element clustering near the sharp excitations can resolve the numerical "noise", where the clustering scheme is repeated for each period of the excitation. However, in cyclic analysis the time-periodic orbit can be computed without marching through the transient solution and element clustering can easily be applied.

3.5.2. Cyclic analysis

The cyclic response of (3.18) can be computed by scaling the physical time t to a scaled time s using the forcing period T

$$\frac{1}{T}\begin{Bmatrix} \dot{u}_2 \\ \vdots \\ \dot{u}_{n-1} \end{Bmatrix} + \mathbf{A}_s \begin{Bmatrix} u_2 \\ \vdots \\ u_{n-1} \end{Bmatrix} = \begin{Bmatrix} -A^*_{(2,1)} f(s) \\ 0 \\ \vdots \\ 0 \end{Bmatrix}, \tag{3.19}$$

where $\dot{u}$ denotes derivative of u with respect to scaled time s and the number of elements of the vector on the right hand side of (3.19) is $n - 2$. The cyclic solution is computed for equal- and clustered-element discretizations at node $n = 2$. In Fig. 3.15a the equal-element solution of $\{N_{el} = 48, m = 5\}$ has numerical "noise" near the rapid variation of the periodic force. To overcome this difficulty, the elements are clustered near $s = \{0, 0.5$ and $1\}$ of the time-cycle. A geometric ratio $r = 1 \times 10^5$ is used in the clustering scheme. The clustering scheme is implemented as shown in Fig. 3.15b and Fig. 3.14b. Though we use the same number of DOFs, see Fig. 3.15b, we note that element clustering has remedied the numerical error due to the rapid variation. Although the long-time analytical solution to (3.16) is not available (within the authors knowledge), the response is expected to resemble the excitation in form as we move towards the left boundary, see Fig. 3.15b. A solution of high-order accuracy can be expected when combined with high order spatial discretization and clustering of elements in time. This was observed in Section 3.2, where 400 DOFs and element clustering provided an accuracy of 10^{-13}, a substantial improvement over the solution obtained with uniform time elements.

The phase plot of the solution at nodes $n = 2$ and 50 is shown in Fig. 3.14b. We observe lack of numerical error when using the element-clustering scheme. We note that in using cyclic analysis we are able to use

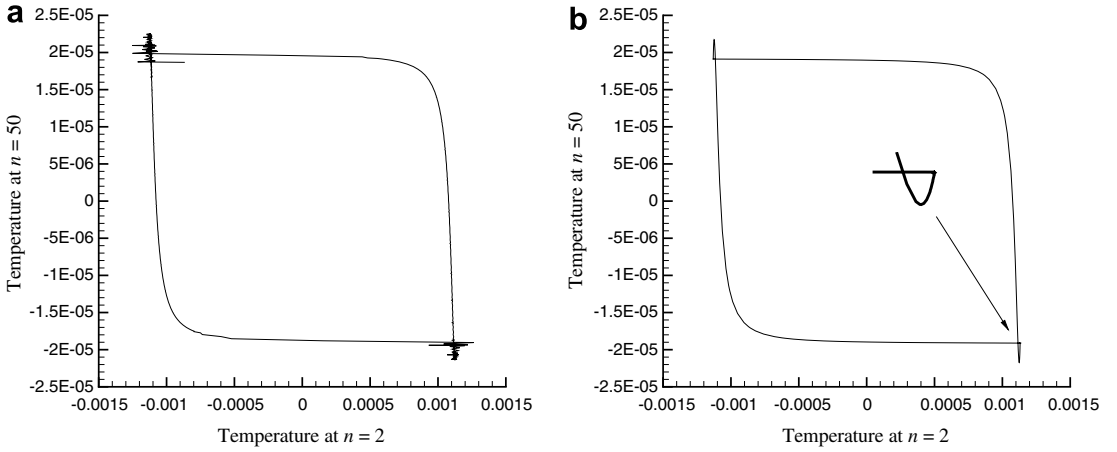

Fig. 3.14. Phase plot for nodes $n = 2$ and $n = 50$: (a) transient response with equal elements at $t = 1.45$; (b) cyclic response with clustered-elements.

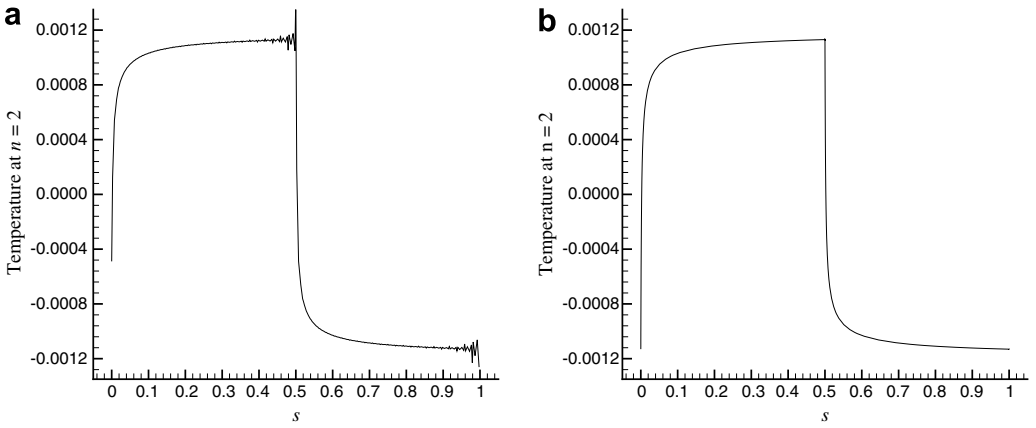

Fig. 3.15. Cyclic response at node 2 for: (a) uniform-element spacing; (b) clustered-element spacing.

element clustering near the rapid variation only once. In the transient solution, see Fig. 3.14a, element clustering would be needed for every period of the solution to alleviate the numerical error due to the rapid variation encountered in every period of the transient solution.

3.6. Hyperbolic partial differential equation

The numerical solution of hyperbolic partial differential equations using standard techniques gives rise to dissipation and dispersion errors. These errors can be traced to wave propagation characteristics of numerical schemes. Dissipation error occurs when the propagated numerical wave amplitude differs from the analytical one, whereas dispersion error is the incorrect phase lag of the propagated numerical wave, which results in spurious oscillations in the solution [56]. To mitigate these errors, specialized numerical schemes are used (see for example [57,58], where a dispersion correction and high-order schemes are used). In this section we demonstrate the low dissipation and dispersion characteristics of the spectral element method in time when applied to hyperbolic problems [25]. An interesting hyperbolic problem is the wave equation, which describes many applications in acoustics, elastodynamics and structural dynamic systems. The equation is composed of second-order derivatives in time and space over the unit-space interval, representing the respective inertial and elastic forces:

$$\left.\begin{aligned} &\tfrac{\partial^2 u}{\partial t^2} = c^2 \tfrac{\partial^2 u}{\partial z^2}, \\ &u(0,t) = f(t) \quad u(1,t) = 0, \\ &u(z,0^-) = g(z) \quad \tfrac{\partial u}{\partial t}(z,0^-) = q(z), \end{aligned}\right\} \tag{3.20}$$

where c is the wave propagation speed. An interesting application of the wave equation is in the reduction of noise in flight cabin through activation of piezoelectric devices at the cabin walls [59]. We demonstrate the dispersion and dissipation characteristics of the spectral element method in time. This is only applied for the transient analysis of the wave equation for two sets of initial and boundary conditions, though the results should be applicable to cyclic analysis.

3.6.1. Spectral discretization in space

In order to conduct a convergence study of hyperbolic problems, the discretizations in both space and time need to be accurate. Consequently, both the space and time domains are discretized using spectral elements. This was previously implemented by many authors, see for example Bar-Yoseph et al. [27], Hulbert and Hughes [28]. First the spatial domain is discretized using spectral elements, then the spectral time discretization is applied. A trial solution in space is written as

$$\hat{u}^{(j)}(\eta,t) = \sum_{k=0}^{m} u^{(j)}(\eta_k,t)\psi_k^{(j)}(\eta), \tag{3.21}$$

where the spatial weighted residual form of (3.20) becomes

$$\sum_{j=1}^{N_{\mathrm{el}}} \int_{-1}^{1} v(\eta)\left[c\frac{2}{h}\frac{\partial^2 \hat{u}^{(j)}}{\partial \eta^2} - \frac{h}{2}\frac{\partial^2 \hat{u}^{(j)}}{\partial t^2}\right] \mathrm{d}\eta = 0, \tag{3.22}$$

and $v(\eta) = \psi_i(\eta)$. After integrating by parts and applying the boundary conditions, the semi-discrete system of ordinary differential equations becomes

$$\mathbf{B}\frac{\mathrm{d}^2 \bar{u}}{\mathrm{d}t^2} = -c\mathbf{D}\bar{u} + c(u^{(1)}(\eta_0, t)\psi_{k,\eta}|_{\eta=-1}\delta_{i0} - u^{(N_{\mathrm{el}})}(\eta_m, t)\psi_{m,\eta}|_{\eta=1}\delta_{im}), \tag{3.23}$$

where the $\bar{u}$ denotes collocation of spatial grid points and the last term consisting of the first and last nodes are known and need not be computed, where $u^{(1)}(\eta_0, t) = f(t)$ and $u^{(N_{\mathrm{el}})}(\eta_m, t) = 0$ and $\mathbf{B}$ and $\mathbf{D}$ are the respective mass and diffusion matrices defined according to

$$\mathbf{B} = \coprod_{k=1}^{N_{\mathrm{el}}}\left[\frac{h}{2}\int_{-1}^{1}\psi_i(\eta)\psi_k(\eta)\mathrm{d}\eta\right], \tag{3.24a}$$

$$\mathbf{D} = \coprod_{k=1}^{N_{\mathrm{el}}}\left[\frac{2}{h}\int_{-1}^{1}\frac{\mathrm{d}\psi_i(\eta)}{\mathrm{d}\eta}\frac{\mathrm{d}\psi_k(\eta)}{\mathrm{d}\eta}\,\mathrm{d}\eta\right]. \tag{3.24b}$$

Here the symbol $\coprod$ refers to the finite-element assembly operator. The inexact integration of (3.24a) using Gauss–Lobatto quadrature leads to a lumped mass matrix $\mathbf{B}$. The final system of equations for a one-element spectral discretization can be written as

$$\mathbf{B}\begin{Bmatrix} u_{tt}(\eta_0, t) \\ \vdots \\ u_{tt}(\eta_m, t) \end{Bmatrix} = -c\begin{pmatrix} D_{(1,1)} - \psi_{k,\eta}|_{\eta=-1} & D_{(1,2)} & \dots & D_{(1,m)} \\ D_{(2,1)} & D_{(2,2)} & \dots & D_{(2,m)} \\ \vdots & \vdots & \dots & \vdots \\ D_{(m,1)} & D_{(m,2)} & \dots & D_{(m,m)} \end{pmatrix}\begin{Bmatrix} u(\eta_0, t) \\ \vdots \\ u(\eta_m, t) \end{Bmatrix}, \tag{3.25}$$

where the boundary conditions are applied to the first and last nodes to yield

$$\mathbf{B}\begin{Bmatrix} u_{tt}(\eta_1, t) \\ \vdots \\ u_{tt}(\eta_{m-1}, t) \end{Bmatrix} = -c\begin{pmatrix} D_{(2,2)} & \dots & D_{(2,m-1)} \\ \vdots & \dots & \vdots \\ D_{(m-1,2)} & \dots & D_{(m-1,m-1)} \end{pmatrix}\begin{Bmatrix} u(\eta_1, t) \\ \vdots \\ u(\eta_{m-1}, t) \end{Bmatrix} - cf(t)\begin{Bmatrix} D(2,1) \\ \vdots \\ D(m-1,1) \end{Bmatrix}. \tag{3.26}$$

The system of second-order differential equations are then transformed to first-order form to facilitate computation of the transient response using the monolithic-time spectral element method.

3.6.2. Transient analysis

We first compute the solution of (3.20) with fixed boundary conditions $f(t) = 0$, zero initial velocity and an initial displacement according to $g(z) = \sin(\pi z)$. The analytical solution for this set of conditions is $u(z, t) = cos(\pi t)\sin(\pi z)$. A high-order discretization in space is used to ensure proper convergence in space with 10 elements and 12th order polynomial. The energy norm of the error is reported in Fig. 3.16a for a fixed number of elements in time, $N_{\mathrm{el}} = 10$, and increasing values of m, and for a fixed polynomial order, $m = 5$, and increasing values of N_{el}. The solution is computed for a time interval of one unit. In the figure, the left and bottom axes refer to the fixed elements case on a semi-log scale. The exponential convergence rate assuming $\gamma = 1$ in (3.3) is noted with the rate equal to $-\beta_m = 4.7$. Furthermore, for $m = 5$, polynomial convergence rate is observed on the double log scale of the right and top axes. Fig. 3.16b reports the transient response for different time snapshots, where the solution exhibits standing waves behavior as described in [52, p. 239].

Next we study the effect of imposing an impulsive boundary condition. The impulse force $f(t)$ is according to (3.5a) with $\epsilon = 0.005$. The analytical solution is $f(t)$ traveling at speed of c in space. To better capture the impulse in space, 20 elements are used (two times larger than previous problem) and 12$^{\mathrm{th}}$ order polynomial. A convergence study of the problem is reported in Fig. 3.17 for a time interval of one unit. Fig. 3.17a indicates

the large accuracy achieved when the polynomial order within each time element is increased. The convergence rate is exponential with $-\beta_m = 2.19$ and $\gamma = 1$. Though the accuracy is limited by round-off error, where increasing the refinement becomes unproductive.

Fig. 3.17b demonstrates the convergence rate for linear and high-order elements when the number of elements is increased. It is seen that for linear elements ($m = 1$), the error continues to decrease; however, unlike the high-order elements, the error remains high even for a large number of DOFs ($N_{\text{el}} = 2000$). To illustrate ingredients of the errors noted above, especially for linear elements, the transient response is computed in Fig. 3.18. The time interval of one unit length is discretized into 101 grid points in time with linear and high-order polynomials. In Fig. 3.18a, the numerical dissipation and dispersion of the linear elements is identified. However, when high-order Lagrange polynomials are used, the dissipation and dispersion errors are greatly reduced; see Fig. 3.18b.

3.7. Standard form with extra weak nonlinearity: cyclic analysis

The applications of the SE method we have discussed so far were all linear. These served to provide a foundational study of the monolithic-time approach for rapid excitations. Though, the method can be applied to nonlinear problems. Examples of previous applications of time-marching spectral element method to nonlinear problems such as the Duffing equation and nonlinear Euler–Bernoulli beam are provided in [17,60]. In this section, we consider the characteristics of the monolithic-time SE solution, when a weak nonlinearity is included in the differential equation without resorting to iterative nonlinear solution methods. In future work we may try build on the analysis provided in references [17,60] to use more effective solvers that exploit the sparseness of the projection matrix.

It is worth to note that for a relatively small disturbances existing nonlinearities in physical systems can be neglected and the linear solution can suffice. However in many cases the nonlinearity can have a stabilizing effect on the system response. Accounting for the nonlinearity would give more accurate prediction of the response. For example ignoring a cubic nonlinearity in flutter of aircraft [61] can give false prediction of flutter wherein limit-cycle oscillations are the correct physical response. To illustrate this we use the following standard form with an additional nonlinear term according to

$$\frac{1}{T}\frac{\mathrm{d}x}{\mathrm{d}s} + ax = G(x, s), \tag{3.27}$$

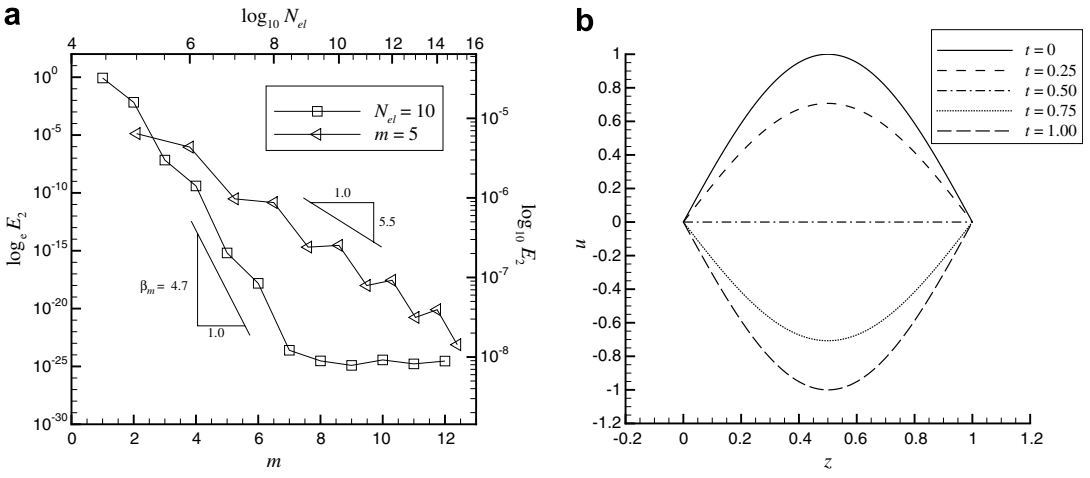

Fig. 3.16. Fixed boundary conditions with an initial displacement, $g(z) = \sin(\pi z)$ for 10 elements in space of order 12: (a) energy norm of error and (b) transient response.

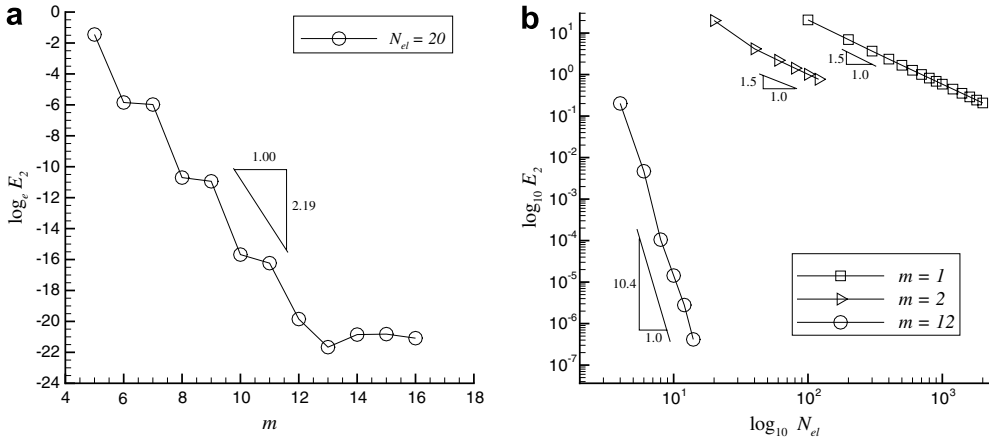

Fig. 3.17. Energy norm of error for an impulsive boundary condition with zero initial conditions for 20 elements in space of order 12; superior accuracy is achieved using high-order elements: (a) exponential convergence rate; (b) polynomial convergence rate.

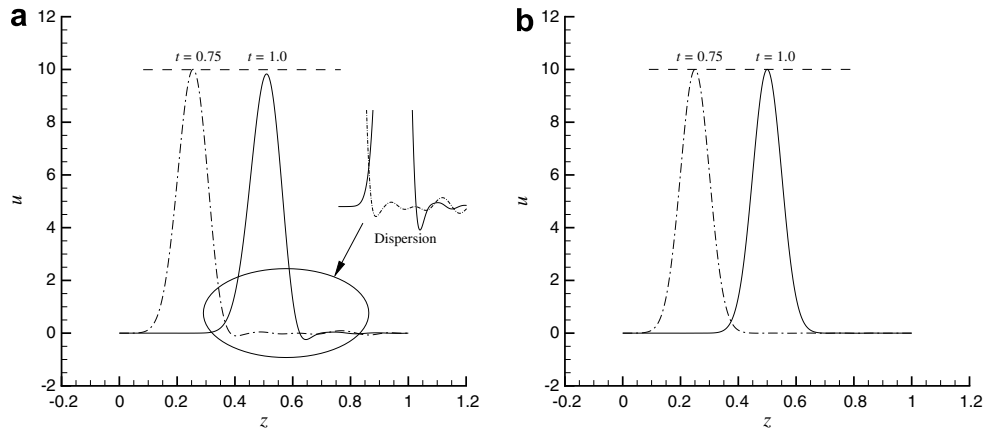

Fig. 3.18. Transient response for an impulsive boundary condition and zero initial conditions: (a) $N_{\mathrm{el}} = 100$ and $m = 1$; (b) $N_{\mathrm{el}} = 20$ and $m = 5$.

where

$$G(x,s) = b\sin 2\pi s - \epsilon(x^2 + \beta x^3),$$

note that we use a weighted form of the forcing function $G(x,s)$ where in (2.15) $G(x,s)$ replaces F.

The linear Jacobian $\mathbf{J}$ can be used to compute the solution to (3.27). We write the residual in (2.22) according to

$$R = \mathbf{L}_{cg}X_{cg} - \mathbf{A}_{cg}X_{cg} + \mathbf{L}_{\omega g}G_{cg}. \tag{3.28}$$

Due to the nonlinearity the solution of (3.28) is iterated according to

$$R^{v+1} = R^{v} + \mathbf{J}\Delta X_{cg} + \mathbf{L}_{\omega g}\left[G_{cg}^{v+1} - G_{cg}^{v}\right]. \tag{3.29}$$

Eq. (3.29) is iterated to zero residual R^{v+1} without calculation of the last term. To facilitate convergence using the linear jacobian $\mathbf{J}$ we use a relaxation parameter λ according to

$$X_{cg}^{v+1} = X_{cg}^{v} + \lambda\Delta X_{cg}. \tag{3.30}$$

The SE solution of (3.27) is computed for the following parameters $a = b = 1$, $T = 0.2$ and $\beta = 50$. In the absence of nonlinearity, see Fig. 3.4, the number of DOFs sufficient to achieve $E = 10^{-11}$ are $\{N_{\mathrm{el}} = 2, m = 12\}$.

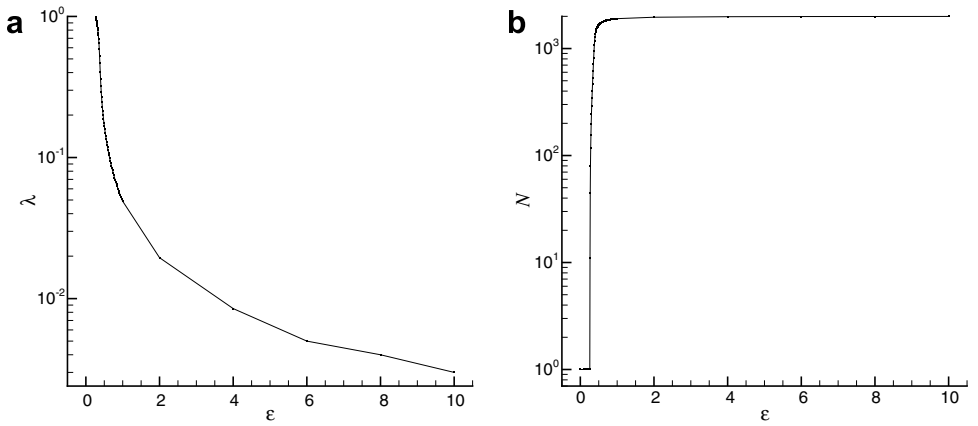

Fig. 3.19. Nonlinear parameter ϵ as a function of (a) relaxation parameter and λ (b) number of iterations, N.

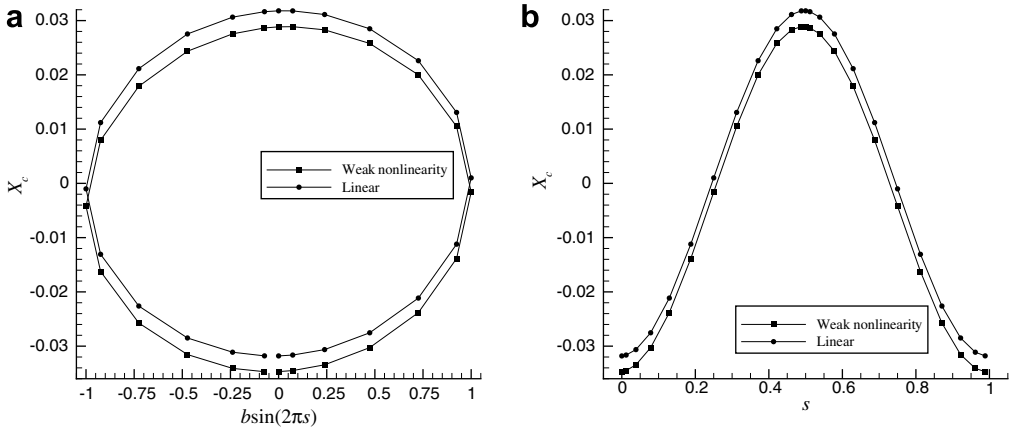

Fig. 3.20. Cyclic response for standard form compared to one with additional weak nonlinearity: (a) periodic orbit of X_c and $b\sin 2\pi s$; (b) X_c as a function of scaled time s.

Using this number of DOFs we study effectiveness of the linear Jacobian, see Fig. 3.19, in computing the solution as the nonlinearity parameter ϵ increases. As noted in Fig. 3.19a, the convergence depends heavily on the relaxation parameter λ, decreasing rapidly as ϵ is increased. The number of iterations N also increases as shown in Fig. 3.19b. In the figure we note that for the linear case ($\epsilon = 0$) only one iteration is needed for convergence with $\lambda = 1$.

For a nonlinearity of $\epsilon = 10$, the SE solution of (3.27) is computed in Fig. 3.20a and b. In Fig. 3.20a the orbit of solution X_c is shown as a function of the harmonic forcing function. The solution is also shown in Fig. 3.20b as a function of scaled time s. Furthermore, in the absence of nonlinearity ($\epsilon = \beta = 0$) the linear solution, computed in Section 3.1.2 is shown in the figure.

4. Numerical implementation

In this section we discuss issues concerned with conditioning and numerical efficiency of SE method in time.

4.1. Conditioning

The numerical solution of a system of equations involves numerical inversion of a matrix. Inexact representation of the matrix leads to an error when the matrix is inverted. This error is amplified when the matrix is

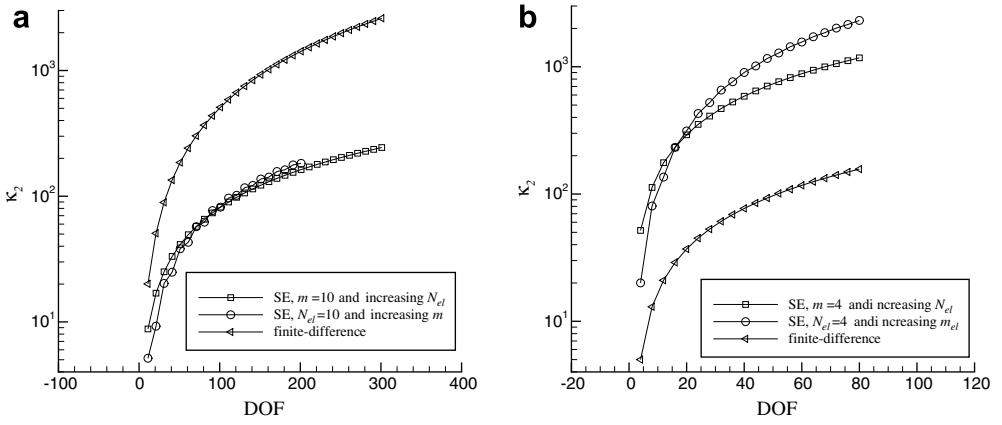

Fig. 4.1. Condition number of the Jacobian matrix versus number of DOFs for SE bases compared to backward finite-difference approximation. (a) Transient-harmonic analysis of first-order differential equation in (3.2). (b) Cyclic-harmonic analysis of first-order differential equation in (3.4).

ill-conditioned. The condition number of a matrix characterizes this amplification and the associated linear independence of the matrix bases. The condition number is defined as, e.g., see [46]

$$\kappa_2 = \|\boldsymbol{\phi}\|_2 \cdot \|\boldsymbol{\phi}^{-1}\|_2 \tag{4.1}$$

where $\|\boldsymbol{\phi}\|_2$ is the matrix L^2 norm of $\boldsymbol{\phi}$. Furthermore, when using iterative techniques to invert the system the number of iterations required to perform the inversion depends on the condition number.

The Jacobian matrix $\mathbf{J}$, see (2.24), represents the SE bases in time, we focus here on first-order problem with harmonic excitation, see Section 3.1. Fig. 4.1 reports the condition number κ_2 of $\mathbf{J}$ as a function of total number of DOFs for transient and cyclic analyses. Additionally, we report the condition number for a Jacobian constructed using an implicit first-order finite-difference approximation in time. This allows comparison of the finite-difference to the spectral element approach with regard to the monolithic-time scheme and helps establish the qualitative difference between cyclic and transient analysis. In Fig. 4.1a we consider transient analysis with a forcing frequency of 5 Hz and $t \in [0,2]$. Two SE cases are considered, where the number of DOFs is increased first by fixing $m = 10$ and increasing $N_{\text{el}} = \{1\text{–}20\}$ second by fixing $N_{\text{el}} = 10$ and increasing $m = \{1\text{–}20\}$. We note here that 10^{-11} accuracy can be achieved using number of DOF = 240 (see Fig. 3.1). The condition number continues to increase when increasing number of DOFs for all cases, however, the rate of increase and value of κ_2 in SE is less than the finite-difference approximation. This makes SE projection in time, for transient analysis, more favorable to conventional finite-difference approach.

In cyclic analysis, see Fig. 4.1b, κ_2 is reported for same forcing frequency and same three cases but with $N_{\text{el}} = 4$ and $m = 4$. Here we note that in contrast to transient analysis, the cyclic/SE condition number is larger than the finite-difference approach. This indicates that the linear independence of the SE bases was more affected (than finite-difference) by applying the cyclic boundary conditions. However, for SE method and considering the number of DOFs necessary to attain 10^{-11} accuracy, we note that κ_2 is equal to 400 and 200 for cyclic and transient analyses, respectively.

4.2. Numerical efficiency

The numerical solution of (2.21) can be handled by direct or indirect methods (iterative). Depending on the structure of the Jacobian matrix (2.24), an efficient method can be selected for solving the system.

As noted earlier in Section 2.2, the global assembly of the differentiation $\boldsymbol{\Psi}$ and weight $\mathbf{I}_\omega$ matrices give the global differentiation $\mathbf{L}_c$ and weight $\mathbf{L}_\omega$ matrices. For transient analysis $\mathbf{L}_c$ and $\mathbf{L}_\omega$ have block-diagonal and diagonal forms, respectively. The final structure of these matrices after global assembly for all dependent variables depends on whether the spatial connectivity matrix $\mathbf{A}_s$, is either coupled, see e.g., (3.17) or uncoupled. Consider the case of uncoupled $\mathbf{A}_s$ for $N_v = 2$. The matrix structure of $\mathbf{L}_{cg}$, $\mathbf{A}_{cg}$ and $\mathbf{J}$ are reported in

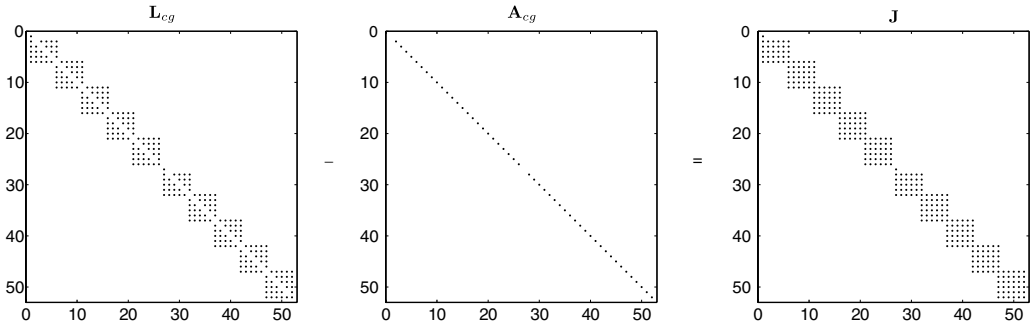

Fig. 4.2. Nonzero elements in transient/SE matrices for a $N_{\mathrm{el}} = 5$, $m = 5$ and $N_v = 2$.

Fig. 4.2 for $\{N_{\mathrm{el}} = 5, m = 5\}$. Direct methods can be used to solve banded matrices, see below for a report of the solution method used. However, for a coupled space–time spectral element method, the resulting global matrices are not banded [27,62]. In these studies splitting methods are used to take advantage of the diagonal nature of the off-diagonal submatrices. The authors indicate the robustness and efficiency of splitting methods with subcycling technique for nonlinear advection–diffusion problems.

For the cyclic analysis, the time-periodic boundary conditions add nonzero elements outside the block form of $\mathbf{L}_c$. This in turn degenerates the banded matrix structure of $\mathbf{J}$ reported in transient analysis. The structure of previous matrices is reported again in Fig. 4.3 for the same parameters but for cyclic boundary conditions.

In the following we report on the computational cost associated with solving (2.23) in the paper. In a next stage of the study, we will consider more efficient solution methods. The matrix inversion in (2.23) is carried using the *backslash* operator in Matlab® and the matrices are assembled in sparse form using *sparse.m*. In general the *backslash* algorithm selects different solution methods depending on the structure of $\mathbf{J}$. We report here on the computational cost associated with the solution of first-order form with harmonic excitation discussed in Section (3.1). However, to report on the computational cost as the problem size grows, we use a decoupled square matrix $\mathbf{A}_{\mathrm{s}}$ of size N_v. The machine used to run the computations has an Intel Xeon processor with a clock frequency of 3.6 GHz.

The transient analysis gives a block-diagonal $\mathbf{J}$, which is of banded form. In this case the *backslash* algorithm selects the LAPACK banded routines which performs an LU decomposition using *DGBTRF* and the system is solved then with *DGBTRS* routine. In the following we use m and N_{el} based on Fig. 3.1. Fig. 4.4a reports the CPU time as a function of total number of N_v for same monolithic-time (2 s) interval specified in Section 3.1.1. The figure indicates a linear increase ($\simeq$1.49) in computational cost as N_v increases.

We compare the computation cost to cyclic analysis. Here, nonzero elements outside the block form disqualifies banded LAPACK routines and the Unsymmetric Multifrontal Package (UMFPACK) [63] is used for solving the system. In Fig. 4.4b the CPU time is reported as a function of N_v. By using UMFPACK, approximately the same computational cost ($\simeq$1.13) is maintained as in transient analysis (although $\mathbf{J}$ is

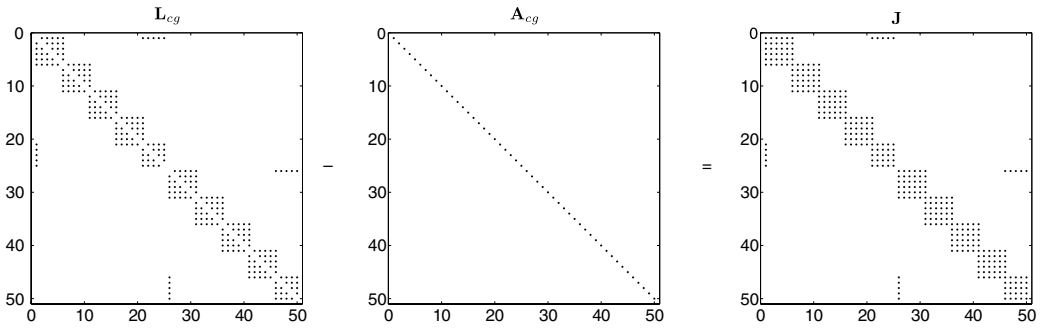

Fig. 4.3. Nonzero elements in cyclic/SE matrices for a $N_{\mathrm{el}} = 5$, $m = 5$ and $N_v = 2$.

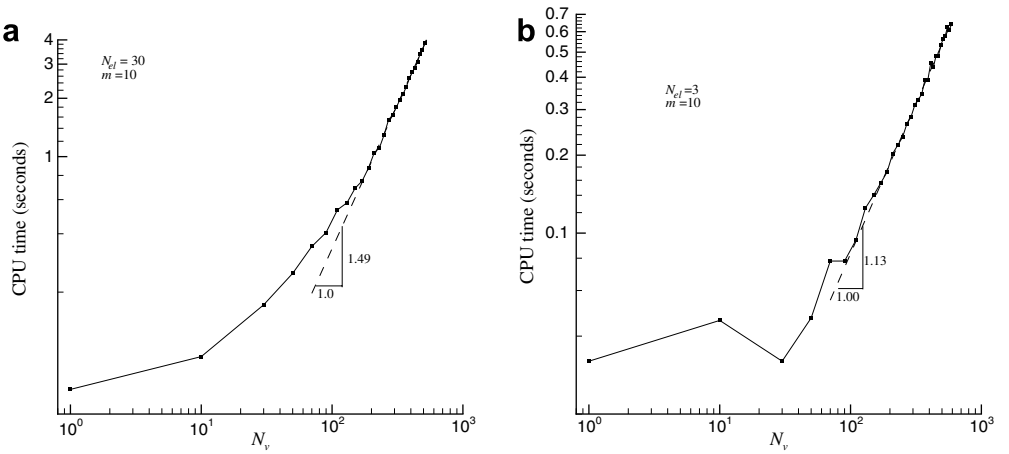

Fig. 4.4. CPU time for first-order system with harmonic excitation. (a) Transient analysis and (b) cyclic analysis.

non-banded) however since the solution is integrated over a single cycle, m and N_{el} need not be too large, see Fig. 3.4, and the computational time is six times smaller.

5. Conclusions

In this paper we applied the SE method in time using a monolithic-time interval (time interval that encompasses transient or converged dynamic solution) computation. In contrast to time-marching, the monolithic-time scheme provides a strong connection between the system dynamics and its parameters. The method was applied to initial value problems and periodically excited differential equations. For periodic excitations, the solution was computed over a single cycle. Periodicity over the cycle was enforced directly on the array of spectral elements. The reduction of the monolithic-time interval to a single cycle eliminated the need for a large number of DOFs to achieve high accuracy.

The method was applied to first-order differential equations with harmonic excitations and excitations admitting rapid transients. The convergence in time of the method was demonstrated. In the case of single harmonic excitation, machine precision was obtained with 25 DOFs per cycle. Additionally, applicability of the method to second-order and fourth-order differential equations was demonstrated. Element clustering was used to handle rapid transients in time. Results showed the anticipated superiority of element clustering over equal-element spacing in time to treat accurately rapid transients. Furthermore, we illustrated the method's low dissipation and dispersion for a second-order hyperbolic problem.

The analysis we presented in the paper served to demonstrate the monolithic-time approach and document its convergence characteristics. This was effectively demonstrated for linear systems. Extension to large systems and/or nonlinear ones needs to be demonstrated and studied with further research. Maintaining the efficiency requires use of more sophisticated solution methods such as multigrid, iterative solvers, and parallelization. It should be noted that the method was successfully applied to a weakly nonlinear problem, but that benchmark nonlinear problems have not yet been examined. In short, the authors believe the SE method in time to have potential for the computation of limit-cycle oscillations in aeroelastic systems, but recognize the need for steps described herein to be altered for the capture of self-sustained dynamics.

The potential for the application of transient or cyclic SE method will ultimately depend on the problem characteristics. The implementation used here allowed for either analysis to be carried after setting the problem in first-order form. The cyclic SE method is well-suited for lightly damped or nonlinear systems exhibiting slow convergence to periodic oscillations, especially for aeroacoustic applications, where long-time integration with low dissipation and dispersion would require large computing time. Though in both the transient and cyclic analyses, the SE method provides a tool that gives sensitivity information directly as a function of the systems parameters. This facilitates design optimization and uncertainty quantification of systems.

Acknowledgements

The authors would like to thank the National Research Council Research Associateship Program and the Air Force Office of Scientific Research under Grant 03VA01COR (Dr. Fariba Fahroo, Program Manager) for financial and logistical support of the research. The authors would like to thank Dr. Gregory Parker for providing the MSC.Nastran finite-element model of the cantilever beam.

References

[1] P. Beran, C. Petit, D. Millman, Uncertainty quantification of limit-cycle oscillations, Journal of Computational Physics 217 (2006) 217–247.
[2] M. Borri, Helicopter rotor dynamics by finite element time approximation, Computers Mathematics with Applications 12A (1) (1986) 149–160.
[3] B. Mann, P. Bayly, M. Davies, J. Halley, Limit cycles, bifurcations, and accuracy of the milling process, Journal of Sound and Vibration 277 (1–2) (2004) 31–48.
[4] M. Kurdi, T. Schmitz, R. Haftka, B. Mann, Milling optimization of removal rate and part accuracy – part 1: Parameter selection, International Journal of Materials Product and Technology, in press.
[5] I. Schreiber, M. Holodniok, M. Kubicek, M. Marek, Periodic and aperiodic regimes in coupled dissipative chemical oscillators, Journal of Statistical Physics 43 (3–4) (1986) 489–519.
[6] M. Kubicek, M. Holodniok, Algorithms for determination of perioddoubling bifurcation points in ordinary differential equations, Journal of Computational Physics 70 (1) (1987) 203–217.
[7] J. Oden, A general theory of finite elements II. applications, International Journal of Numerical Methods in Engineering 1 (1969) 247–259.
[8] C. Desai, J. Oden, L. Johnson, Evaluation and analyses of some finite element and finite difference procedures for time-dependent problems AEWES-Misc-Paper-S-75-7 (1975) 10. Available at: <http://stinet.dtic.mil/oai/oai/>. Accession number: ADA009739.
[9] I. Fried, Finite element analysis of time-dependent phenomena, AIAA Journal 7 (1969) 1170–1173.
[10] J. Argyris, D. Scharpf, Finite elements in time and space, Nuclear Engineering and Design 10 (4) (1969) 456–464.
[11] K. Palaniappan, P. Beran, A. Jameson, Optimal control of LCOs in aerostructural systems, AIAA Paper 2006-1621, May 1–4.
[12] S. Nadarajah, A. Jameson, Optimum shape design for unsteady flows with time-accurate continuous and discrete adjoint methods, AIAA Journal 45 (2007) 1478–1491.
[13] A. Patera, A spectral element method for fluid dynamics; laminar flow in a channel expansion, Journal of Computational Physics 54 (1984) 468–488.
[14] R. Riff, M. Baruch, Time finite element discretization of Hamilton's law of varying action, AIAA Journal 22 (1984) 1310–1318.
[15] D. Aharoni, P. Bar-Yoseph, Mixed finite element formulations in the time domain for solution of dynamic problems, Computational Mechanics 9 (1992) 359–374.
[16] P. Bar-Yoseph, Time finite element methods for initial value problems, Applied Numerical Mathematics 33 (1–4) (2000) 435–445.
[17] P. Bar-Yoseph, D. Fisher, O. Gottlieb, Spectral element methods for nonlinear temporal dynamical systems, Computational Mechanics 18 (4) (1996) 302–313.
[18] T. Tezduyar, M. Behr, J. Liou, New strategy for finite element computations involving moving boundaries and interfaces. The deforming-spatial domain/space–time procedure. I. The concept and the preliminary numerical tests, Computer Methods in Applied Mechanics and Engineering 94 (3) (1992) 339–351.
[19] T. Tezduyar, S. Sathe, R. Keedy, K. Stein, Space–time finite element techniques for computation of fluid–structure interactions, Computer Methods in Applied Mechanics and Engineering 195 (17–18) (2006) 2002–2027.
[20] J. Pontaza, J. Reddy, Space–time coupled spectral/hp least-squares finite element formulation for the incompressible Navier–Stokes equations, Journal of Computational Physics 197 (2) (2004) 418–459.
[21] B. Bell, K. Surana, A space–time coupled p-version least squares finite element formulation for unsteady two-dimensional Navier–Stokes equations, International Journal for Numerical Methods in Engineering 39 (15) (1996) 2593–2618.
[22] C. Klaij, J. van der Vegt, H. van der Ven, Space–time discontinuous Galerkin method for the compressible Navier–Stokes equations, Journal of Computational Physics 217 (2) (2006) 589–611.
[23] C. Klaij, J. van der Vegt, H. van der Ven, Pseudo-time stepping methods for space–time discontinuous Galerkin discretizations of the compressible Navier–Stokes equations, Journal of Computational Physics 219 (2) (2006) 622–643.
[24] J. van der Vegt, H. van der Ven, Space–time discontinuous Galerkin finite element method with dynamic grid motion for inviscid compressible flows. I. General formulation, Journal of Computational Physics 182 (2) (2002) 546–585.
[25] P. Bar-Yoseph, Space–time discontinuous finite element approximations for multi-dimensional non-linear hyperbolic systems, Computational Mechanics 5 (1989) 145–160.
[26] P. Bar-Yoseph, E. Moses, Space–time spectral element methods for unsteady convection–diffusion problems, International Journal of Numerical Methods for Heat and Fluid Flow 7 (2–3) (1997) 215–235.
[27] P. Bar-Yoseph, E. Moses, U. Zrahia, A. Yarin, Space–time spectral element methods for one-dimensional nonlinear advection–diffusion problems, Journal of Computational Physics 119 (1) (1995) 62–74.
[28] G. Hulbert, T. Hughes, Space–time finite element methods for second-order hyperbolic equations, Computer Methods in Applied Mechanics and Engineering 84 (1990) 327–348.

[29] E. Fehlberg, Classical fifth-, sixth-, seventh-, and eighth-order Runge–Kutta formulas with step size control, NASA Technical Report, 1968, pp. 1–82.
[30] N. Newmark, A method of computation for structural dynamics, ASCE Journal of the Engineering Mechanics Division 5 (EM3) (2002) 67–94.
[31] H. Hilber, T. Hughes, R. Taylor, Improved numerical dissipation for time integration algorithms in structural dynamics, Earthquake Engineering and Structural Dynamics 5 (1977) 283–292.
[32] J. Yao, A. Jameson, J. Alonso, F. Liu, Development and validation of a massively parallel flow solver for turbomachinery flows, Journal of Propulsion and Power 17 (3) (2001) 659–668.
[33] B. Cockburn, C.-W. Shu, Runge–Kutta discontinuous Galerkin methods for convection-dominated problems, Journal of Scientific Computing 16 (3) (2001) 173–261.
[34] M. Giles, Stability analysis of a Galerkin/Runge–Kutta Navier–Stokes discretisation on unstructured tetrahedral grids, Journal of Computational Physics 132 (2) (1997) 201–214.
[35] N. Nikitin, Third-order-accurate semi-implicit Runge–Kutta scheme for incompressible Navier–Stokes equations, International Journal for Numerical Methods in Fluids 51 (2) (2006) 221–233.
[36] D.J. Doedel, AUTO: A program for the automatic bifurcation analysis of autonomous systems, in: 10th Manitoba Conference on Numerical Mathematics and Computation, vol. 30, University of Manitoba, Winnipeg, Canada, 1981, pp. 265–284.
[37] M. Holodniok, M. Kubicek, DERPER–an algorithm for the continuation of periodic solutions in ordinary differential equations, Journal of Computational Physics 55 (2) (1984) 254–267.
[38] R. Paffenroth, E. Doedel, D. Dichmann, Continuation of periodic orbits around lagrange points and AUTO2000, Advances in the Astronautical Sciences 109 I (2002) 41–60.
[39] E. Doedel, W. Govaerts, Y. Kuznetsov, Computation of periodic solution bifurcations in ODEs using bordered systems, SIAM Journal on Numerical Analysis 41 (2) (2003) 401–435.
[40] A. Gopinath, A. Jameson, Time spectral method for periodic unsteady computations over two- and three- dimensional bodies, AIAA Paper 2005-1220, January 10–13.
[41] K. Hall, J. Thomas, W. Clark, Computation of unsteady nonlinear flows in cascades using a harmonic balance technique, AIAA Journal 40 (5) (2002) 879–886.
[42] J. Thomas, E. Dowell, K. Hall, Modeling viscous transonic limit-cycle oscillation behavior using a harmonic balance approach, Journal of Aircraft 41 (6) (2004) 1266–1274.
[43] A. Gopinath, A. Jameson, Application of the time spectral method to periodic unsteady vortex shedding, AIAA Paper 2006-0449, January 9–12.
[44] A.K. Gopinath, P. Beran, A. Jameson, Comparative analysis of computational methods for limit-cycle oscillations, AIAA Paper 2006-2076, May 1–4.
[45] F. Schilder, W. Vogt, S. Schreiber, H.M. Osinga, Fourier methods for quasi-periodic oscillations, International Journal for Numerical Methods in Engineering 67 (5) (2006) 629–671.
[46] G. Karniadakis, S. Sherwin, Spectral/hp Element Methods for CFD, Oxford University Press, 1999.
[47] C. Pozrikidis, Introduction to Finite and Spectral Element Methods Using Matlab, Chapman and Hall/CRC, 2005.
[48] D. Burnett, Finite Element Analysis; From Concepts to Applications, Addison-Wesley, 1988.
[49] B. Szabo, I. Babuska, Finite Element Analysis, John Wiley and Sons, 1991.
[50] R. Steidel, An Introduction to Mechanical Vibrations, John Wiley and Sons, 1989.
[51] M. Blair, G. Parker, P. Beran, R. Snyder, A computational design framework for flapping micro air vehicles, AIAA Paper 2007-0763, January 09—14.
[52] L. Meirovitch, Elements of Vibration Analysis, McGraw-Hill, 1986.
[53] R. Cook, D. Malkus, M. Plesha, R. Witt, Concepts and Applications of Finite Element Analysis, John Wiley and Sons, 2002.
[54] K. Gupta, J. Meek, Finite element multidisciplinary analysis, AIAA Education Series, 2003.
[55] MSC.Nastran software corporation, 2 MacArthur Place Sanata Ana, CA 92707, MSC.Nastran basic dynamic analysis: Users guide, 2005.
[56] L. Lapidus, G. Pinder, Numerical Solution of Partial Differential Equations in Science and Engineering, Wiley-Interscience, Princeton, New Jersey, 1982.
[57] S. Krenk, Dispersion-corrected explicit integration of the wave equation, Computer Methods in Applied Mechanics and Engineering 191 (8–10) (2001) 975–987.
[58] T. Schwartzkopff, C. Munz, E. Toro, ADER: A high-order approach for linear hyperbolic systems in 2D, Journal of Scientific Computing 17 (1–4) (2002) 231–240.
[59] I. Lasiecka, R. Marchand, Control and stabilization in nonlinear structural acoustic problems, Proceedings of the SPIE – The International Society for Optical Engineering 3039 (1997) 192–203.
[60] P. Bar-Yoseph, D. Fisher, O. Gottlieb, Spectral element methods for nonlinear spatio-temporal dynamics of an Euler–Bernoulli beam, Computational Mechanics 19 (2) (1996) 136–151.
[61] B. Lee, L. Jiang, Flutter of an airfoil with a cubic nonlinear restoring force, AIAA Paper 98-1725, April 20–23.
[62] P. Bar-Yoseph, D. Elata, Efficient L2 Galerkin finite element method for multi-dimensional non-linear hyperbolic systems, International Journal for Numerical Methods in Engineering 29 (6) (1990) 1229–1245.
[63] T. Davis, Unsymmetric MultiFrontal PACKage (UMFPACK) Version 4.6, University of Florida, Gainesville. URL <http://www.cise.ufl.edu/research/sparse/umfpack>, 2005.